

# Structural Stability of Clean, Passivated, and Partially Dehydrogenated Cuboid and Octahedral Nanodiamonds Up to 2 Nanometers in Size

Denis Tarasov<sup>1</sup>, Ekaterina Izotova<sup>2</sup>, Diana Alisheva<sup>2</sup>,  
Natalia Akberova<sup>2</sup>, and Robert A. Freitas, Jr.<sup>3,\*</sup>

<sup>1</sup>Kazan Branch of Joint Supercomputer Center, Russian Academy of Sciences, Kazan, 420111, Russia

<sup>2</sup>Department of Biochemistry, Kazan State University, Kazan, Tatarstan, 420008, Russia

<sup>3</sup>Institute for Molecular Manufacturing, Palo Alto, CA 94301, USA

The use of precisely applied mechanical forces to induce site-specific chemical transformations is called positional mechanosynthesis, and diamond is an important early target for achieving mechanosynthesis experimentally. The next major experimental milestone may be the mechanosynthetic fabrication of atomically precise 3D structures, creating readily accessible diamond-based nanomechanical components engineered to form desired architectures possessing superlative mechanical strength, stiffness, and strength-to-weight ratio. To help motivate this future experimental work, the present paper addresses the basic stability of the simplest nanoscale diamond structures—cubes and octahedra—possessing clean, hydrogenated, or partially hydrogenated surfaces. Computational studies using Density Functional Theory (DFT) with the Car-Parrinello Molecular Dynamics (CPMD) code, consuming ~1,466,852.53 CPU-hours of runtime on the IBM Blue Gene/P supercomputer (23 TFlops), confirmed that fully hydrogenated nanodiamonds up to 2 nm (~900–1800 atoms) in size having only C(111) faces (octahedrons) or only C(110) and C(100) faces (cuboids) maintain stable sp<sup>3</sup> hybridization. Fully dehydrogenated cuboid nanodiamonds above 1 nm retain the diamond lattice pattern, but smaller dehydrogenated cuboids and dehydrogenated octahedron nanodiamonds up to 2 nm reconstruct to bucky-diamond or onion-like carbon (OLC). At least three adjacent passivating H atoms may be removed, even from the most graphitization-prone C(111) face, without reconstruction of the underlying diamond lattice.

**Keywords:** Carbon, Cuboid, Bucky-Diamond, Diamond, Dehydrogenation, DFT, Dimerization, DMS, Fullerene, Hydrogen, Mechanosynthesis, Nanodiamond, Nanotechnology, Octahedron, OLC, Reconstruction, Stability.

## CONTENTS

1. Introduction . . . . .	1
1.1. Clean Nanocarbon . . . . .	3
1.2. Fully Hydrogenated Nanocarbon . . . . .	4
1.3. Partially Dehydrogenated Nanocarbon . . . . .	5
2. Computational Methods . . . . .	8
3. RESULTS AND DISCUSSION . . . . .	9
3.1. Clean and Hydrogenated Nanodiamond Octahedrons . . . . .	9
3.2. Clean and Hydrogenated Nanodiamond Cuboids . . . . .	13
3.3. Dimerization Patterns on Nanodiamond C(100) Faces . . . . .	14
3.4. Partial Dehydrogenation of Nanodiamond Surfaces . . . . .	15
4. Conclusions . . . . .	19
Acknowledgments . . . . .	19
References . . . . .	19

## 1. INTRODUCTION

Arranging atoms in most of the ways permitted by physical law is a fundamental objective of molecular manufacturing. A more modest and specific objective is the ability to synthesize atomically precise diamondoid structures using positionally-controlled molecular tools. Such positional control might be achieved using an instrument like a Scanning Probe Microscope (SPM).

The use of precisely applied mechanical forces to induce site-specific chemical transformations using positionally-controlled highly reactive tools is called positional mechanosynthesis. In 2008, Freitas and Merkle<sup>1</sup> reviewed all known theoretical studies of positional diamond mechanosynthesis (DMS). They proposed the first

\*Author to whom correspondence should be addressed.

complete set of DMS reaction sequences and an associated minimal set of nine specific SPM-based DMS tooltips operating in vacuum that could be used to build cubic and hexagonal diamond lattices of process-unlimited size, graphene sheets (e.g., carbon nanotubes) and polyynes chains, and all of the tools themselves including all necessary tooltip recharging reactions, virtually atom by atom, using only the elements C, Ge and H. In 2009 Tarasov et al.<sup>2</sup> completed the first extensive DMS tooltip trajectory analysis, examining a wide range of viable multiple

degrees-of-freedom tooltip motions in 3D space that could be employed to recharge the hydrogen abstraction tool, a key reaction set in DMS.

The landmark experimental demonstration of positional atomic assembly occurred in 1989 when Eigler and Schweizer<sup>3</sup> employed an SPM to spell out the IBM logo using 35 xenon atoms arranged on nickel surface, though no covalent bonds were formed. In 2003, Oyabu et al.<sup>4</sup> achieved the first experimental demonstration of atomically precise purely mechanical positionalchemical



**Denis Tarasov** is Senior Research Scientist at the Kazan Branch of Joint Supercomputer Center, Russian Academy of Sciences, in Kazan, Russia. He graduated from the Department of Biochemistry of Kazan State University in Kazan (Russian Federation) and received an M.S. in biochemistry. He was awarded his Ph.D. in Biology from Kazan State University in 2004. His research interests include computer modeling in biology and chemistry, high performance computing, and molecular machine systems. He has 15 refereed journal publications.



**Ekaterina Izotova** is a Ph.D. candidate in Kazan State University with research interests in molecular mechanics and quantum chemistry methods. She was born in Kazan (Russia) and received her M.S. in biochemistry from Kazan State University.



**Diana Alisheva** is a Ph.D. candidate at the Kazan State University with research interests in molecular mechanics, quantum chemistry and computer graphics for scientific visualization. She was born in Kazan (Russia) and received her M.S. in biochemistry from Kazan State University.



**Natalia Akberova** is Assistant Professor of the Kazan State University biology department. She has a Ph.D. in Biology, with specialization in biochemistry (1999) and lecturer of courses for biology department students in informatics, bioinformatics, and modeling in biology. Her scientific interests include systems biology, bioinformatics, and molecular modeling.



**Robert A. Freitas, Jr.** is Senior Research Fellow at the Institute for Molecular Manufacturing (IMM) in Palo Alto, California, and was a Research Scientist at Zyvex Corp. (Richardson, Texas), the first molecular nanotechnology company, during 2000–2004. He received B.S. degrees in Physics and Psychology from Harvey Mudd College in 1974 and a J.D. from University of Santa Clara in 1979. Freitas authored in 1996 the first detailed technical design study of a medical nanorobot ever published in a peer-reviewed mainstream biomedical journal, followed by *Nanomedicine* (Landes Bioscience, 1999, 2003; [www.nanomedicine.com](http://www.nanomedicine.com)), the first book-length technical discussions of the potential medical applications of molecular nanotechnology. He has 49 refereed publications, serves on the Editorial Boards of 9 medical or nanotech journals, co-authored the book *Kinematic Self-Replicating Machines* (Landes Bioscience, 2004; [www.molecularassembler.com/KSRM.htm](http://www.molecularassembler.com/KSRM.htm)), co-founded in 2006

the Nanofactory Collaboration ([www.molecularassembler.com/Nanofactory](http://www.molecularassembler.com/Nanofactory)) to build the first working nanofactory for atomically precise manufacturing, won the 2009 Feynman Prize in nanotechnology for theory, and in 2010 was awarded the first U.S. patent on diamond mechanosynthesis. His home page is at [www.rfreitas.com](http://www.rfreitas.com).

synthesis on a heavy atom using only mechanical forces to make and break covalent bonds, first abstracting and then rebonding a single silicon atom to a silicon surface with SPM positional control in vacuum at low temperature. Using an atomic force microscope the same group similarly manipulated individual Ge atoms in 2004 and Si/Sn and Pb/In atoms in 2008.<sup>5,6</sup>

The next major experimental milestone may be the mechanosynthetic fabrication of atomically precise 3D structures, creating readily accessible diamond-based nanomechanical components engineered to form desired architectures possessing superlative mechanical strength, stiffness, and strength-to-weight ratio. These nanoscale components may range from relatively simple diamond cubes, rods or rings to more sophisticated “nanoparts” such as fullerene bearings,<sup>7–9</sup> gears<sup>10–12</sup> and motors,<sup>13</sup> composite fullerene/diamond structures,<sup>14</sup> and more complex devices<sup>15</sup> such as diamondoid gears,<sup>16</sup> pumps,<sup>16</sup> and conveyors.<sup>17</sup> To help motivate this future experimental work, the present paper addresses the basic stability of the simplest nanoscale diamond structures—cubes and octahedra—possessing clean, hydrogenated, or partially hydrogenated surfaces.

### 1.1. Clean Nanocarbon

Macroscale diamond has long been known to be thermodynamically stable with respect to graphite only at high pressure. At room temperature and pressure, graphite is stable but diamond is only metastable with respect to graphite—that is, the diamond is slowly graphitizing. Room-temperature diamond is only  $\sim 0.02$  eV ( $\sim k_B T$ ) higher in energy than graphite but a large activation barrier inhibits the transformation,<sup>18</sup> so macroscale diamond, once formed near or below room temperature, will not readily transform into graphite. However, for a sufficiently small carbon cluster, nanodiamond can be more stable than nanographite because of the small molar volume of diamond compared to that of graphite.<sup>19</sup> As particle size falls

deeper into the nanoscale, graphite and diamond phases can sometimes co-exist with, or even be co-opted by, other forms of pure carbon, particularly (A) onion-like carbon or OLC (multi-shelled nested fullerenes)<sup>20</sup> and (B) “bucky-diamond” (a diamond core up to a few nanometers wide surrounded by a partially or completely delaminated fullerene outer shell),<sup>21</sup> an intermediary between nanodiamond and OLC. There appear to be three distinct thermodynamic regimes for pure carbon nanoparticles as a function of size:<sup>19,22</sup>

- (1) The size range above 5–10 nm is most likely the graphitic regime wherein the graphite phase is thermodynamically preferred and the nanodiamond phase is metastable relative to graphite, but where nanodiamond, once formed (e.g., from  $sp^3$ -bonded amorphous carbon clusters),<sup>23</sup> will not readily transform into graphite at moderate or low temperatures in any practical time period.
- (2) The size range from 1.5–2 nm up to 5–10 nm is the nanodiamond regime in which the diamond phase is thermodynamically the most stable form for pure carbon nanoparticles. Gamarnik<sup>24,25</sup> used a thermodynamic model to calculate the size-dependent threshold preference for stable pure carbon nanodiamond over nanographite as 10.2 nm at 25 °C, 6.1 nm at 545 °C, 4.8 nm at 800 °C, and 4.3 nm at 1100 °C. Jiang et al.<sup>26</sup> modeled the phase transition thermodynamics between nanodiamond and nanographite including the effects of surface stress on the internal pressure of the nanoparticle, and found the transition size to nanodiamond decreases from  $\sim 11$  nm at 0 K to  $\sim 4$  nm at 1500 K; they note the experimental observation that 5 nm nanodiamonds are transformed into nanographite at 1073 K. (Carbon implantation experiments<sup>27</sup> also suggest that diamond is the stable form of carbon for crystallites  $< 7$  nm that are appropriately surface passivated.) Winter and Ree<sup>28,29</sup> used primarily empirical (PM3 and AM1 Hartree-Fock) models to predict that small nanodiamond clusters formed in the detonation of high explosives are more stable than graphite below approximately 33,000–70,000 atoms (depending upon the

computational method used), corresponding to a particle size of 6–8 nm; in another study using other methods, Barnard et al.<sup>22</sup> estimated 24,398 atoms (~5.2 nm) as the upper limit. Note that this size range for nanodiamond stability does not represent the only size regime in which nanocrystalline diamond may be formed; it simply indicates that outside of this range the nanodiamonds will be metastable with respect to a transformation to graphitic or fullerene phases.<sup>19</sup>

(3) The nanoparticle size range of 1.5–2 nm and smaller is the fullerene regime, in which pure carbon nanoparticles will spontaneously form OLC or else the diamond and fullerene phases will co-exist as bucky-diamonds. A DFT (Density Functional Theory)-based study by Wen et al.<sup>30</sup> found that the crossover from  $sp^3$  (nanodiamond) to  $sp^2$  (fullerene) stability occurs at  $n_{\text{carbon}} \sim 1060$  atoms (~2.1 nm). Barnard et al.<sup>22</sup> also investigated the phase stability of these smaller nanocarbon particles by modeling the enthalpy of formation for relaxed, dehydrogenated (stable) nanodiamond crystals and fullerenes. The results indicated crossover to a more stable fullerene phase below ~1100 atoms, equivalent to cubic nanodiamond crystals ~1.9 nm in diameter and corresponding roughly to the experimentally observed minimum nanodiamond particle size;<sup>31</sup> this cutoff size was later confirmed by Barnard and Sternberg<sup>32</sup> using DFTB (density functional based tight binding). A review<sup>33</sup> of the literature regarding the structure of carbon nanoparticles indicates that other carbon forms such as fullerenes and onion-like carbon (OLC) are abundant at sizes below 1.8 nm. For example, one comparison<sup>34</sup> of the relative stability of 60–540 atom fullerenes and closed carbon nanotubes using first-principles pseudopotential calculations, predicted (in agreement with experimental observations) that a ~1.3 nm diameter nanotube is energetically preferred among the various SWNTs and fullerenes examined. Note that phase transitions in a coexistence regime<sup>35</sup> are not entirely thermodynamically driven; other factors such as surface energies, surface stress and charge, and kinetic considerations including direct mechanochemical forces may be instrumental in inducing a change of phase.<sup>19</sup>

There are three sub-regimes within the fullerene regime.<sup>35</sup> In the range of 500–900 atoms (~1.4–1.7 nm), OLC is the most stable form of pure nanocarbon; from 900–1350 atoms (~1.7–2.0 nm), bucky-diamond and OLC coexist; and between 1350–1850 atoms (~2.0–2.2 nm), bucky-diamond and nanodiamond coexist. The intersection of the bucky-diamond and OLC stability was found to be very close to the intersection for nanodiamonds and fullerenes at ~1100 atoms (~1.9 nm), suggesting that above this size an  $sp^3$ -bonded core becomes more favorable than a  $sp^2$ -bonded core, irrespective of surface structure.<sup>35</sup> It was also determined using semiempirical<sup>36</sup> and first principles methods<sup>37</sup> that the nanodiamond-to-onion phase transition is initiated by the presence of the

diamond C(111) surface, and does not occur on the C(110) and C(100) surfaces.<sup>38</sup>

A related study by Barnard and Snook<sup>39</sup> found that single-walled carbon nanotubes are the most energetically preferred form for 1-D pure nanocarbon structures, but that there may exist a narrow window of stability for nonhydrogenated diamond nanowires between about 450 atoms (2.7 nm diameter) and 870–930 atoms (3.7–3.9 nm) per unit length. *Ab initio* analysis shows that the C(110) and C(100) surfaces of diamond nanowires remain stable in the  $sp^3$  configuration<sup>40</sup> (though exhibiting significant changes in the length and cross-sectional area) but the C(111) surfaces delaminate to form nano-tubular cages, running parallel to the nanowire axis, called “bucky-wires” (analogous to bucky-diamonds),<sup>41</sup> with chiral structures identical to that of an armchair carbon nanotube.<sup>42</sup>

## 1.2. Fully Hydrogenated Nanocarbon

In the case of fully-hydrogenated carbon nanoparticles, the addition of passivating hydrogen atoms is not expected to reduce the preferential stability of nanodiamonds in the 1.5–2.0 nm up to 5–10 nm size range or the metastability of nanodiamonds relative to nanographite in the 5–10 nm and larger size range. The remaining uncertainty pertains to the smallest size range, ~2 nm and below.

In 2003 Raty and Galli<sup>43</sup> used first-principles calculations (based on formation energy, with terms for the vibrational and the total energy of a nanoparticle obtained using DFT) to examine the relative stability of <2 nm nanodiamonds as a function of surface hydrogenation. By comparing various degrees of hydrogen coverage for five ~spherical particle sizes containing 29 (~0.6 nm), 66 (~0.8 nm), 147 (~1.2 nm), 211 (~1.3 nm), and 275 (~1.4 nm) carbon atoms, the difference in formation energy between particles with dehydrogenated surfaces and particles with hydrogenated surfaces was found to decrease as the size of the nanoparticle increases, but not depending significantly on the hydrogen chemical potential.<sup>43</sup> These results suggest that as nanodiamond size is reduced below about 2–3 nm, bucky-diamonds may become energetically preferred even to fully hydrogenated nanodiamonds of the same size because the  $sp^2$  fullerene shell is lower in energy than a hydrogenated diamond surface. However, this study did not adequately account for the difference in chemical potential between “core” atoms and the reconstructed “bucky” surface atoms.<sup>19</sup> Raty and Galli also note that their analysis is relevant to CVD synthesis conditions (i.e., far from equilibrium). It remains unknown if their results are applicable to the growth of nanodiamond under continuous near-equilibrium conditions during DMS.

In contrast to the Raty and Galli<sup>43</sup> results, numerous other computational studies show that <2 nm fully-hydrogenated diamond nanoparticles are stable under

ambient (or low) pressure and temperature conditions. For example:

(1) In 1998 Winter and Ree<sup>28</sup> used the AM1 and PM3 parameterizations of the semi-empirical modified neglect of diatomic overlap (MNDO) method to optimize the geometry of diamond clusters ( $C_{10}$ ,  $C_{35}$ ,  $C_{84}$ ,  $C_{165}$ , and  $C_{286}$  octahedral nanodiamonds), both for pure carbon forms and for structures whose dangling bonds were capped with hydrogen. In all cases, the surface instability observed after relaxing the dehydrogenated clusters was eliminated, the diamond structure was preserved throughout, and the optimized (relaxed) H-passivated diamond clusters gave  $sp^3$  C–C bond lengths very close to the experimental value of 1.54 Å.

(2) Similar results were obtained by Barnard et al.<sup>37,44</sup> in 2003 as part of a more rigorous first-principles study of cubic ( $C_{28}H_{32}$ ,  $C_{54}H_{48}$ , and  $C_{259}H_{140}$ ), octahedral ( $C_{35}H_{36}$ ,  $C_{84}H_{64}$ , and  $C_{165}H_{100}$ ), and cuboctahedral ( $C_{29}H_{24}$ ,  $C_{142}H_{72}$ , and  $C_{323}H_{124}$ ) nanodiamonds up to ~1 nm in diameter. Calculations were performed with VASP using DFT within the generalized gradient approximation (GGA) and the Perdew-Wang (PW91) exchange-correlation functional with ultrasoft, gradient-corrected, Vanderbilt-type pseudopotentials. Comparison of the carbon framework of the relaxed dehydrogenated and hydrogenated versions of the same nanodiamonds confirms that hydrogenated octahedrons are stable at 0 K with hydrogenation eliminating the transformation to bucky-diamond, and that H-passivated nanodiamonds are characterized by more bulk-diamond-like properties such as cohesive energy<sup>44</sup> and surface structure.<sup>38</sup> (All octahedron faces are C(111) crystal planes, the surface most prone to graphitization.) The retention of  $sp^3$  bonding in the passivated nanodiamonds was confirmed via calculation of Wannier functions (local bond-centered functions rather than atom-centered ones)—dehydrogenated structures contained distorted  $\sigma$ - and  $\pi$ -bonds while their hydrogenated counterparts were found to be entirely  $\sigma$ -bonded<sup>44,45</sup>—and via DFT (VASP) in a related study.<sup>42</sup>

(3) In 2004, Barnard<sup>46</sup> showed that hydrogenation eliminates C(111) surface delamination of diamond nanowires. Hydrogenation of the cuboctahedral  $C_{168}H_{72}$  and octahedral  $C_{186}H_{96}$  diamond nanowire surfaces reduced the expansions and contractions of the nanowire segment length and cross-sectional area exhibited by their dehydrogenated ( $C_{168}$  and  $C_{186}$ ) counterparts.<sup>41</sup> Hydrogenation even stabilized otherwise unstable B- and N-doped cuboctahedral ( $C_{29}H_{24}$ ) and Al-, O-, and P-doped cubododecahedral (cylindrical) ( $C_{63}H_{36}$ ) diamond nanowire segments.<sup>47,48</sup>

(4) In 2005, Laikov and Ustynyuk<sup>49</sup> benchmarked PRIRODA-DFT using the fully-hydrogenated nanodiamond tetrahedrons  $C_{26}H_{32}$ ,  $C_{51}H_{52}$ ,  $C_{87}H_{76}$ ,  $C_{136}H_{104}$ ,  $C_{200}H_{136}$ ,  $C_{281}H_{172}$  and  $C_{381}H_{212}$  (~2 nm edge), and found no indication of lattice reconstruction.

(5) In 2006, Lewandowski and Merchant<sup>50</sup> found that hydrogenating 1.2–1.8 nm diamond nanowires, simulated at 300 K using Car-Parrinello Molecular Dynamics, removes all mechanical flexibility and stabilizes the diamond structure.

(6) In 2007, Wen et al.<sup>30</sup> applied all-electron DFT calculations to a series of hydrogenated octahedrons up to  $C_{455}H_{196}$ , finding these structures to be stable and possessing a negative heat of formation (i.e., exothermic) for  $n_{\text{carbon}} < 752$  atoms (~1.9 nm). As the hydrogenated nanodiamond size increased, the average C–C bond length rose slightly from 1.5407 Å for  $C_{35}H_{36}$  (0.7 nm) to 1.5432 Å for  $C_{455}H_{196}$  (1.7 nm), slowly approaching the C–C bond length of 1.5471 Å for bulk diamond crystal at the PW91/DNP level of theory.<sup>30</sup>

Experimentally, there are many examples of very stable and very small  $sp^3$ -bonded hydrogen-terminated carbon nanoparticles in the ~1 nm range, in particular the hydrocarbon cage molecules known as “diamondoids” that occur in natural petroleum, from single-cage adamantane ( $C_{10}H_{16}$ ) to the multi-cage polymantanes (e.g., 11-cage undecamantane, ~100 atoms, ~1 nm).<sup>51</sup> An experimental study found that hydrogen termination of 2–20 nm nanodiamond crystallites prevents their graphitization under extreme UV irradiation.<sup>52</sup> Plasma hydrogenation of multi-walled carbon nanotubes converts them to bucky-diamond, the core becoming cubic or hexagonal nanodiamond depending on the relative chiralities of the innermost nanotube shells.<sup>53</sup> Barnard<sup>19</sup> suggests that even if H-terminated nanodiamonds were slightly higher in energy than their dehydrogenated counterparts, the nanodiamonds might still be metastable below the hydrogen desorption temperature, thus preventing spontaneous (size-dependent) hydrogen desorption and recombination in the absence of a suitable kinetic factor such as the activation energy required for hydrogen desorption.

Pragmatic experimentalists sometimes complain that nanodiamonds oxidize and that fully (or partially) hydrogenated surfaces are unrealistic, but nanodiamonds in the DMS context are intended to be fabricated in a largely oxygen-free UHV environment using a controlled sequence of 1-, 2- or 3-atom site-specific mechanosynthetic transfers from an atomically precise tooltip. In computational nanoscience, H is a generic passivant atom and the stability of the underlying lattice structure of a nanodiamond depends almost entirely on the general presence or absence of passivation, and far less on the nature of the specific passivating species used.

### 1.3. Partially Dehydrogenated Nanocarbon

The effect of partial dehydrogenation on nanoparticle stability has yet to be seriously addressed. During DMS, one or two neighboring radical sites must be created on a growing passivated nanodiamond workpiece (e.g., by removing

one or two H atoms using a positionally-controlled hydrogen abstraction tool) in preparation for the next step in a DMS reaction sequence for building diamond lattice—such as the site-specific addition of a methyl group to the new radical site, or the use of radical–radical coupling to bond two radical sites, using another positionally-controlled DMS tool.

Cubic diamond has three principal or high-symmetry cleavage planes—the C(110), C(100) and C(111) crystallographic faces.

The clean C(110)–(1 × 1) diamond surface (Fig. 1(A)), which consists of zigzag chains of carbon atoms having some  $\pi$ -bond character (bondlength  $\sim 1.43$  Å),<sup>54</sup> does not reconstruct after annealing even to  $>1300$  K<sup>55</sup> though such high temperatures may begin to induce graphitization.<sup>56</sup> Heating the hydrogen-terminated C(110)–H(1 × 1) surface (Fig. 1(B)) to  $>1400$  K yields a dehydrogenated “clean” but unreconstructed C(110)–(1 × 1) surface,<sup>57</sup> with the C–C bondlength in the zigzag chain increasing to 1.51 Å.<sup>54</sup> Hence partial dehydrogenation of passivated C(110) should not cause lattice reconstruction.

The clean C(100)–(1 × 1) diamond surface (Fig. 1(C)) has two dangling bonds per exposed carbon atom, an unstable surface that immediately reconstructs to a C(100)–(2 × 1) pentagonal-ring geometry via the formation of rows of symmetric  $\pi$ -bonded (double-bonded) dimers.<sup>58</sup>

(Graphitization of C(100) occurs readily  $>1600$  K<sup>59</sup> but is more difficult than for C(110).<sup>60</sup>) Addition of 1 H atom per dimer carbon atom, a 1.0 ML (monolayer) surface coverage, increases dimer bondlength from 1.37 Å (C=C) to 1.61 Å (C–C) but leaves the existing lattice reconstruction intact (Fig. 1(D)).<sup>58</sup> (In theory a dihydride (2.0 ML) could de-reconstruct the C(100) surface but its existence is controversial, and the monohydride may be energetically preferred and more stable against spontaneous CH<sub>4</sub> formation;<sup>61</sup> 1.25 ML,<sup>62</sup> 1.33 ML,<sup>63</sup> 1.5 ML,<sup>58</sup> 1.75 ML,<sup>62</sup> and other polyhydrides<sup>62,64</sup> have also been proposed.) Partial dehydrogenation of monohydride-passivated C(100)–H(2 × 1) surface should not alter the existing lattice reconstruction geometry.

A clean C(111) diamond surface that is passivated with a saturated monolayer (1.0 ML) of H atoms exhibits a stable C(111)–H(1 × 1) monohydride hexagonal lattice structure (Fig. 1(E)) that does not reconstruct at room temperature.<sup>65</sup> Upon heating in vacuo sufficiently to remove the passivating hydrogen ( $\sim 800$ – $1100$  K),<sup>66</sup> the carbon atoms at the C(111)–(1 × 1) “shuffle plane” (one dangling bond per exposed tri-bonded carbon atom) surface undergo reconstruction into a new stable sp<sup>2</sup> bonding structure with C(111)–(2 × 1) symmetry called

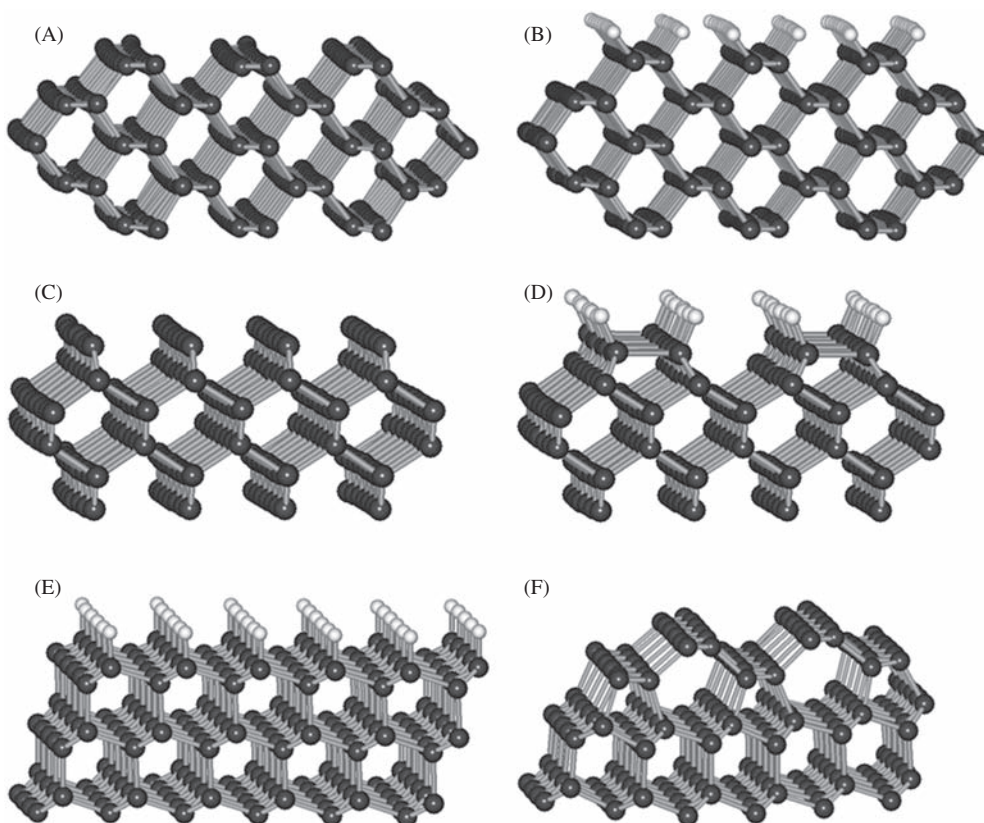


**Fig. 1.** Principal diamond surfaces: (A) C(110)–(1 × 1); (B) C(110)–H(1 × 1); (C) unstable C(100)–(1 × 1); (D) reconstructed C(100)–H(2 × 1); (E) C(111)–H(1 × 1) glide plane; (F) C(111)–(2 × 1) Pandey reconstruction. (C = black, H = white).

the Pandey reconstruction,<sup>67</sup> a rearrangement energetically favored by 0.3–0.7 eV<sup>68,69</sup> with a low or zero transition barrier.<sup>70</sup> In the Pandey reconstruction (Fig. 1(F)), the puckered-hexagon layer of the ideal (111) surface is transformed into planar zigzag chains of carbon atoms, alternately raised and lowered, in a conformation not unlike the ideal (110) surface. The connectivity to the next layer of underlying atoms is affected, with the formation of alternating five- and seven-membered rings<sup>71</sup> and  $\pi$ -bonded chains arising in the first upper two layers<sup>67</sup> (which use up the unsatisfied valencies or dangling bonds). Further heating of the Pandey surface causes graphitization,<sup>69</sup> the separation of the uppermost layer from the lower layers analogous to bucky-diamond, whereas rehydrogenation recovers the original C(111)–H(1 × 1) surface (i.e., Pandey reconstruction is reversible).

Uncertainty exists in the experimental literature about the exact threshold fraction of hydrogen surface coverage—e.g., 0.50 ML,<sup>72–74</sup> 0.33 ML,<sup>78</sup> 0.20 ML,<sup>79</sup> or

less<sup>74–77</sup>—required to suppress all Pandey reconstruction of the C(111) surface and maintain the  $sp^3$  (1 × 1) structure across the entire surface. A first-principles dynamical simulation by Jackson<sup>80</sup> of two adjacent dangling carbon bonds on an otherwise hydrogen-saturated diamond C(111) surface, using a simple cluster model, provided early theoretical evidence that two adjacent dangling surface bonds might be stable (i.e., a localized 0.33 ML threshold). The study found that the two dangling-bond carbon atoms relaxed slightly into the surface, enhancing their bonding with the subsurface carbon atoms and shortening their bond lengths to these atoms from 1.54 Å to 1.41 Å, while at the same time the two dangling-bond carbon atoms showed no tendency to enhance their bonding to each other which could lead to surface reconstruction. A subsequent study by Barnard et al.<sup>42</sup> performed with VASP using DFT and GGA/PW91 with ultrasoft, gradient-corrected, Vanderbilt-type pseudopotentials examined the re-lamination of an exfoliated C(111) surface consisting

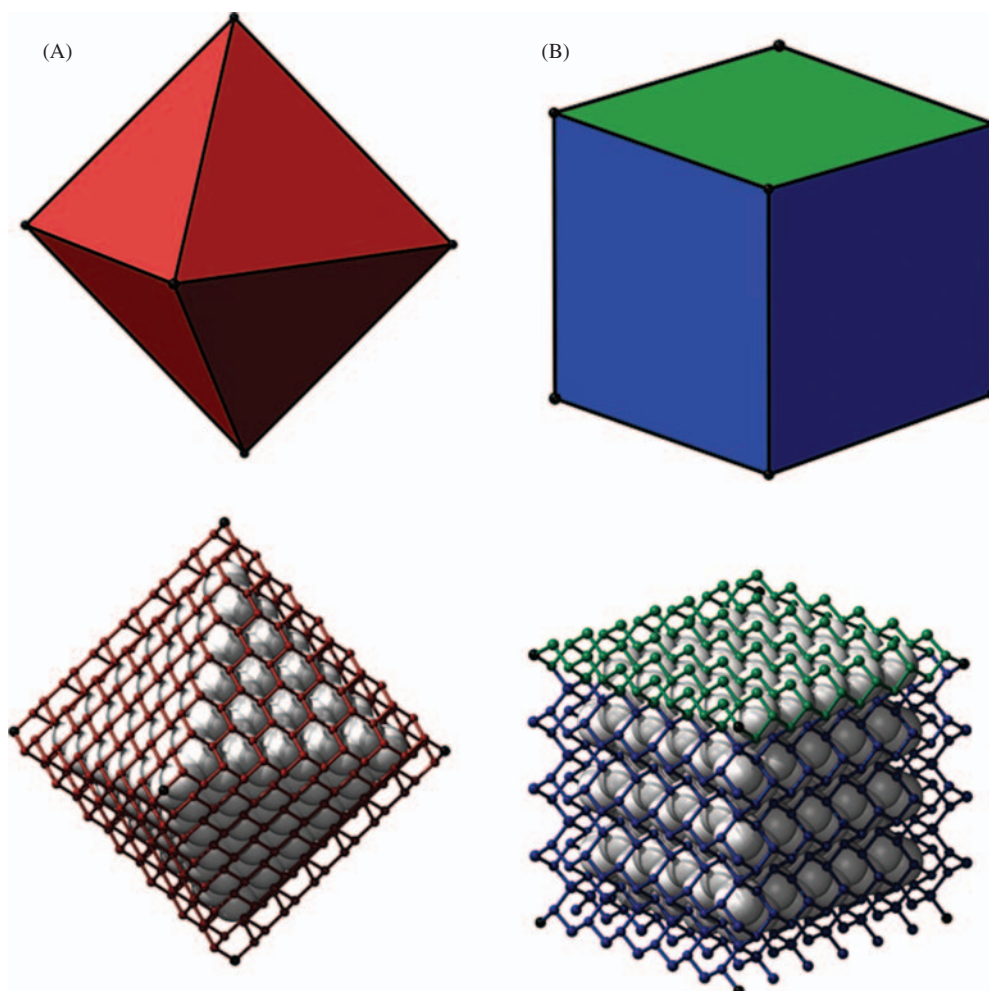


**Fig. 2.** Schematic representations of initial un-relaxed structures cleaved from a diamond lattice, showing examples of (A) octahedral (all C(111) faces) and (B) cuboid (C(110) and C(100) faces) shapes. For clarity, only un-reconstructed surface atoms are shown in the wire-frame images (bottom), where the color (red = C(111), blue = C(110), green = C(100)) corresponds to the crystallographic orientation as indicated by the geometric images (top); redrawn from Barnard and Sternberg;<sup>32</sup> images courtesy Damian G. Allis, Syracuse University.

of a diamond slab 12 atomic layers thick and an exfoliated sheet 2 atomic layers thick onto which single atomic hydrogens were successively but randomly chemisorbed. Re-lamination of the sheet reaches  $\sim 100\%$   $sp^3$  bonding at 0.50–0.60 ML, suggesting that removing one passivating H atom from a C(111)–H( $1 \times 1$ ) surface during DMS should not disrupt the diamond lattice; the re-laminating sheet reaches  $\sim 60\%$   $sp^3$  at  $\sim 0.33$  ML, so a lattice-nondisruptive removal of two adjacent H atoms on C(111)–H( $1 \times 1$ ) also seems possible.

## 2. COMPUTATIONAL METHODS

Graphitization of nanodiamond to form bucky-diamond, bucky-wire or OLC is least likely on C(110) and C(100) faces and most likely on C(111) faces, so our study of structural stability focuses on nanoparts of two kinds. At the one extreme is structures having cuboid (or, equivalently, rectangular prism) geometry (Fig. 2(A)). These can be designed using only C(110) and C(100) faces and no C(111) faces, hence should present the easiest case for nanodiamond stability. At the other extreme is structures having octahedral geometry consisting entirely of C(111)

faces and no C(110) or C(100) faces (Fig. 2(B)), representing the greatest challenge for nanodiamond stability.

The initial structures for a representative series of octahedral and cuboid nanodiamond “nanoparts” up to 2 nm in size (Table I) were carved from a larger diamond slab that was energy-minimized using MM+ in HyperChem. The octahedrons are well-defined in size and shape because C(111) is the natural cleavage plane and all faces are of the same type. The cuboids are not exactly perfect cubes because two different crystal faces intersect, hence there is choice in the precise number of atomic layers and in the termination geometries to be employed for the C(100) faces at the top and bottom of each cuboid. Keeping all 3 dimensions as equal as possible, a series of 13 cuboids were produced by rotating the diamond lattice until a tessellation pattern appeared from above the C(100) plane, then counting the number of squares along each edge defining the nanodiamond in this plane (e.g., Cube15  $\times$  15 results from carving out a chunk of lattice measuring 15 squares on an edge). Each square is roughly half the width of an adamantane cage. For all 13 cuboids and 7 octahedrons, both hydrogenated and unhydrogenated cases, we computed the minimum energy geometry and examined the results for changes in bond length, structural

**Table I.** Cuboid and octahedron nanodiamonds.

Cuboids						Octahedra				
File name	Total # atoms	Chemical formula	Dimensions (Å)			File name	Total # atoms	Chemical formula	Dimensions (Å)	
			X	Y	Z				Edge	Diagonal
Dehydrogenated (clean) diamond						Dehydrogenated (clean) diamond				
Cube3 $\times$ 3	21	C <sub>21</sub>	3.7	3.9	5.5	Octa2 $\times$ 2	10	C <sub>10</sub>	2.5	3.6
Cube4 $\times$ 4	46	C <sub>46</sub>	4.8	5.1	5.5	Octa4 $\times$ 4	35	C <sub>35</sub>	5.1	7.1
Cube5 $\times$ 5	65	C <sub>65</sub>	6.2	6.3	7.0	Octa6 $\times$ 6	84	C <sub>84</sub>	7.5	10.6
Cube6 $\times$ 6	104	C <sub>104</sub>	7.5	7.5	7.0	Octa8 $\times$ 8	165	C <sub>165</sub>	10.1	14.2
Cube7 $\times$ 7	168	C <sub>168</sub>	8.8	8.9	8.7	Octa10 $\times$ 10	286	C <sub>286</sub>	12.6	17.8
Cube8 $\times$ 8	246	C <sub>246</sub>	9.9	10.0	10.5	Octa12 $\times$ 12	455	C <sub>455</sub>	15.1	21.4
Cube9 $\times$ 9	297	C <sub>297</sub>	11.1	11.3	10.5	Octa14 $\times$ 14	680	C <sub>680</sub>	17.7	25.0
Cube10 $\times$ 10	428	C <sub>428</sub>	12.6	12.6	12.8					
Cube11 $\times$ 11	600	C <sub>600</sub>	13.9	13.9	14.1					
Cube12 $\times$ 12	693	C <sub>693</sub>	15.1	15.1	14.1					
Cube13 $\times$ 13	891	C <sub>891</sub>	16.4	16.5	16.0					
Cube14 $\times$ 14	1167	C <sub>1167</sub>	17.6	17.7	17.8					
Cube15 $\times$ 15	1328	C <sub>1328</sub>	19.0	19.0	17.8					
Fully passivated (hydrogenated) diamond						Fully passivated (hydrogenated) diamond				
Cube3 $\times$ 3H	47	C <sub>21</sub> H <sub>26</sub>	5.6	5.7	7.3	Octa2 $\times$ 2H	26	C <sub>10</sub> H <sub>16</sub>	4.3	5.0
Cube4 $\times$ 4H	94	C <sub>46</sub> H <sub>48</sub>	6.8	6.8	7.4	Octa4 $\times$ 4H	71	C <sub>35</sub> H <sub>36</sub>	6.8	8.5
Cube5 $\times$ 5H	117	C <sub>65</sub> H <sub>52</sub>	8.1	8.3	9.0	Octa6 $\times$ 6H	148	C <sub>84</sub> H <sub>64</sub>	9.4	12.1
Cube6 $\times$ 6H	180	C <sub>104</sub> H <sub>76</sub>	9.4	9.4	9.0	Octa8 $\times$ 8H	265	C <sub>165</sub> H <sub>100</sub>	12.0	15.7
Cube7 $\times$ 7H	272	C <sub>168</sub> H <sub>104</sub>	10.6	10.7	10.9	Octa10 $\times$ 10H	400	C <sub>286</sub> H <sub>114</sub>	14.5	19.3
Cube8 $\times$ 8H	380	C <sub>246</sub> H <sub>134</sub>	11.9	11.9	12.5	Octa12 $\times$ 12H	651	C <sub>455</sub> H <sub>196</sub>	17.0	22.9
Cube9 $\times$ 9H	445	C <sub>297</sub> H <sub>148</sub>	13.3	13.3	12.5	Octa14 $\times$ 14H	936	C <sub>680</sub> H <sub>256</sub>	19.6	26.5
Cube10 $\times$ 10H	628	C <sub>428</sub> H <sub>200</sub>	14.8	14.8	14.3					
Cube11 $\times$ 11H	852	C <sub>600</sub> H <sub>252</sub>	15.9	15.9	16.2					
Cube12 $\times$ 12H	965	C <sub>693</sub> H <sub>272</sub>	17.1	17.2	16.2					
Cube13 $\times$ 13H	1211	C <sub>891</sub> H <sub>320</sub>	18.4	18.5	18.1					
Cube14 $\times$ 14H	1571	C <sub>1167</sub> H <sub>404</sub>	19.7	19.7	20.4					
Cube15 $\times$ 15H	1760	C <sub>1328</sub> H <sub>432</sub>	21.0	21.0	20.4					

rearrangements, graphitization, or other evidence of structural instability.

For C(100) surfaces on cuboids with an even number of north-south dimerizable rows (Fig. 1(C)), fabrication via positionally-controlled DMS allows the surface to be manufactured with a uniform pattern of dimers such that all dangling bonds are consumed (Fig. 1(D))—presumably the global minimum on the PES. This is not possible for C(100) cuboid faces having an odd number of north-south dimerizable rows (Cube6 × 6H, Cube10 × 10H, and Cube14 × 14H) because in such cases one north-south row will be unpaired, giving rise to a variety of possible dimerization patterns. To determine the energetically preferred dimerization pattern, we performed structure optimizations on all dimerization patterns for Cube6 × 6H (3 north-south rows and 2 east-west rows, giving 2 unique permutations of 2 dimers and 2 solitaires) and for Cube10 × 10H (5 north-south rows, 4 east-west rows, 10 unique permutations of 8 dimers and 4 solitaires). Similar analysis of Cube14 × 14H (7 north-south rows, 6 east-west rows, 72 unique permutations of 18 dimers and 6 solitaires) was impractical with available computational resources. Taking 0 = dimer in leftmost position and 1 = dimer shifted right by one row, then for Cube6 × 6H the 2 unique combinations may be denoted as: 00 (=11) and 01 (=10). For Cube10 × 10H the 10 unique combinations may be denoted as: 0000, 1000 (=0001), 0100 (=0010), 1100 (=0011), 1010 (=0101), 1001, 0110, 1110 (=0111), 1101 (=1011), and 1111.

To determine the sensitivity of hydrogenated nanodiamond lattice structure to selective single-atom depassivation, from 1 to up to 5 neighboring H atoms were removed in specific patterns from several representative surface locations on C(100)–H(2 × 1) and C(110)–H(1 × 1) faces of Cube8 × 8H and on a C(111)–H(1 × 1) face of Octa12 × 12H. In another series of runs, surface H atoms were successively removed from a center location on each of the three principal crystal planes, in closest proximity to previously created radical sites to observe the threshold local depassivation required to trigger significant change in the local diamond lattice structure. Another series looked at neighboring depassivations from vertex locations. For partial depassivations the smallest possible multiplicity was used in most cases, i.e., singlet for even –H deletions and doublet for odd –H deletions.

All studies were conducted using DFT consuming ~1,466,852.53 CPU-hours of runtime on the IBM Blue Gene/P supercomputer (23 TFlops) installed at Moscow State University, plus 24,000 CPU hours on the JS20 cluster (PowerPC 970FX CPUs). Most calculations were performed using the Car-Parrinello Molecular Dynamics (CPMD) code,<sup>81</sup> a parallelized plane-wave/pseudopotential implementation of DFT particularly designed for ab-initio molecular dynamics. Computations were done using BLYP (Becke, Lee, Yang, Parr) and PBE (Perdew, Burke,

Ernzerhof)<sup>82</sup> functionals within the generalized-gradient approximation (GGA) and ultrasoft, gradient-corrected, Vanderbilt-type pseudopotentials with a kinetic energy plane-wave cutoff of 340 eV using a cubic periodic supercell in which at least 4 Å of clearance was left between any atom and the periodic cell boundary, giving >8 Å separation between periodic images. (The more common B3LYP is a hybrid functional containing a Hartree-Fock exchange component, impractical for molecules with extremely large atom counts.) A few calculations were also performed using the PRIRODA quantum chemistry code<sup>49</sup> that can do fast DFT calculations using the resolution-of-the-identity (RI) approximation to the Hartree-Fock method, supporting RI-MP2 (second-order Møller-Plesset)<sup>83</sup> and coupled-cluster CCSD and CCSD(T) with analytical gradients. In PRIRODA, DFT PBE and MP2 methods were used with the L1 basis set<sup>84</sup> which is an analog of the cc-VDZ basis set. Since the PBE functional gave closer match to experiment than BLYP in preliminary tests on ten of the smallest structures, PBE was used almost exclusively for the remaining larger structures. Note that “C####” in Section 3.4 refers to a specific carbon atom in a referenced nanodiamond model available in the supplemental structure files.

### 3. RESULTS AND DISCUSSION

#### 3.1. Clean and Hydrogenated Nanodiamond Octahedrons

Geometry optimizations of the octahedral nanodiamonds yielded the following results:

Octa2 × 2H (adamantane). Does not reconstruct (all methods) (Fig. 3(A)). In this and other cases below, BLYP overestimates the C–C bond length by ~0.02 Å (1.56 Å) whereas PBE (CPMD, PRIRODA) gives values close to experiment (1.54 Å).

Octa2 × 2. For the dehydrogenated adamantane cage, geometry optimization using PBE produces a rearranged closed-cage structure possessing three 3-member rings (all but one bondlengths 1.43–1.46 Å), three 5-member rings (all but one bondlengths 1.43–1.46 Å), and one 6-member ring (Fig. 3(B)) with the topmost carbon pair at 1.698 Å, indicating 10% bond strain; the structure is mostly sp<sup>2</sup>, apparently fullereneized. BLYP produces the same structure but with the topmost carbon pair debonded (Fig. 3(C)).

Octa4 × 4H (Fig. 3(D)), Octa6 × 6H (Fig. 3(H)). Does not reconstruct (all methods).

Octa4 × 4. CPMD-PBE optimization converges to the very slightly rounded shape as reported by Barnard et al.<sup>37</sup> for C<sub>35</sub> crystal with the perimeter bondlengths contracting to 1.44–1.46 Å (vs. 1.41 Å from Barnard et al.<sup>37</sup>; indicating trend toward sp<sup>2</sup>) and bondlengths to the central atom extend to 1.63–1.65 Å (vs. 1.60 Å from Barnard et al.<sup>37</sup>; indicating increasing sp<sup>3</sup> bond strain) (Fig. 3(E)). However, we found that this state (Octa4 ×

4-config1) is only metastable. (The PRIRODA-PBE optimization also passes through this state, but then the central atom loses its privileged position and bonds to an outer wall atom—and the choice of outer wall atom determines the final result.) A short molecular dynamics simulation of Octa4 × 4-config1 in CPMD (48 fs, 300 K) produced another metastable rearrangement (Octa4 × 4-config2) whose energy is lower (CPMD-PBE:  $-6.96$  eV,

PRIRODA-HF:  $-6.27$  eV, PRIRODA-MP2:  $-12.2$  eV) than Octa4 × 4-config1 after subsequent optimization (Fig. 3(F)). Continuing this MD annealing process finally yielded an apparently stable rearrangement (Octa4 × 4-config3) whose energy is even lower (CPMD-PBE:  $-18.71$  eV, PRIRODA-HF:  $-25.57$  eV, PRIRODA-MP2:  $-27.48$  eV) than Octa4 × 4-config1 after subsequent optimization (Fig. 3(G)). The structure shown is a hollow

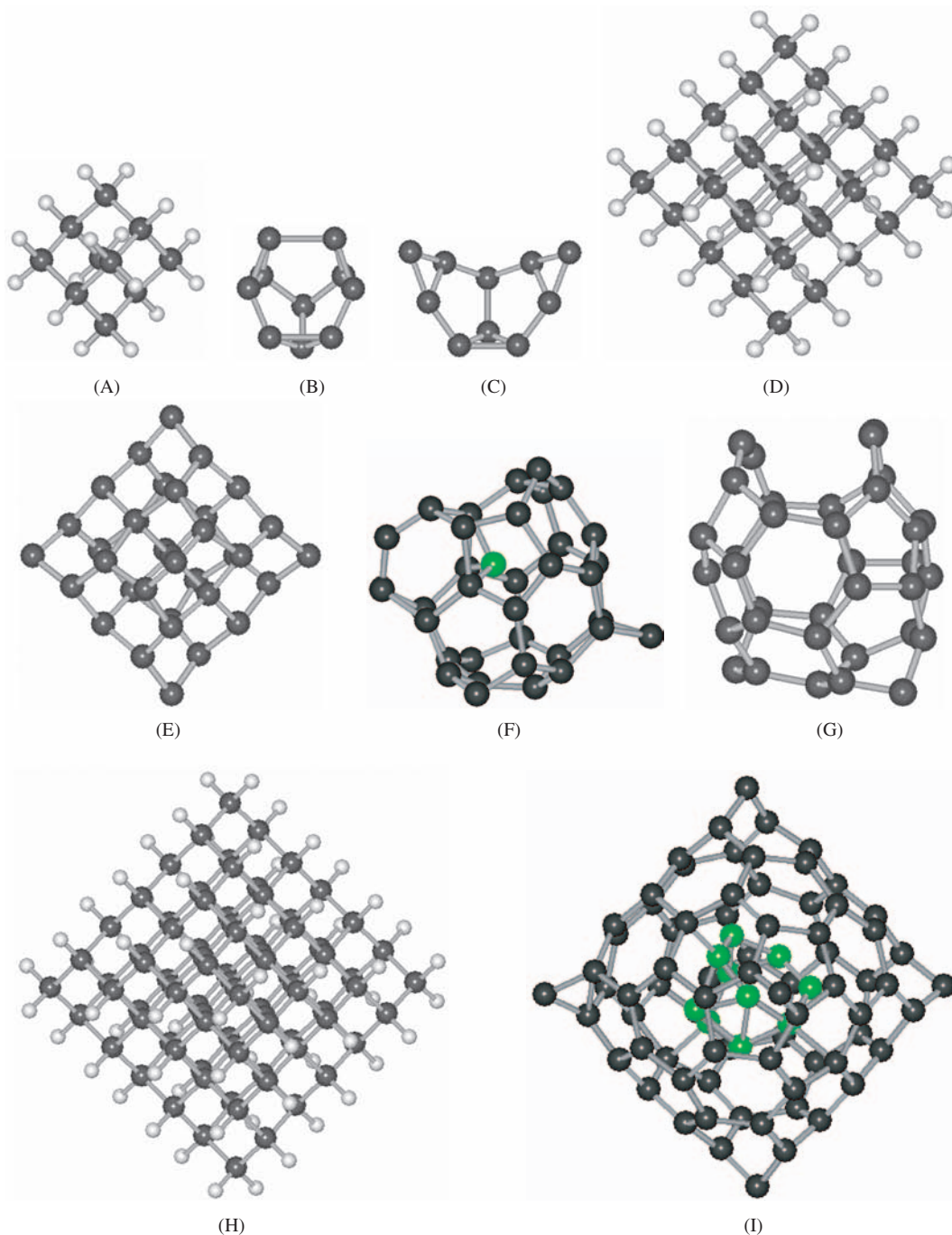


**Fig. 3.** Octahedron, side views: (A) Octa2 × 2H (adamantane) (PBE), (B) Octa2 × 2 (PBE), (C) Octa2 × 2 (BLYP), (D) Octa4 × 4H (PBE), (E) Octa4 × 4-config1 (PBE), (F) Octa4 × 4-config2 (PBE), (G) Octa4 × 4-config3 (PBE), (H) Octa6 × 6H (PBE), and (I) Octa6 × 6 (PBE). (C = black, H = white, Core C Atoms = green).

fullerene shell (no endohedral atoms) consisting predominantly of 6-carbon rings, but including one 5-carbon ring, one 7-carbon ring, and one 11-carbon ring (incorporating two 1.25–1.26 Å C≡C bonds at the top) defining the open-mouth top of the basket. Relative energy differences are large because so many bonds are involved in rearrangements, and because the initial structure is far from the global minimum and many local minima are available nearby. A normal modes analysis to verify a global minimum was not attempted because the PES is very complex, the three minima identified so far are probably not directly connected, and CPMD does not offer the IRC method and has no tools to simplify transition state location analogous to Gaussian QSTN. Optimizing Octa4 × 4 using CPMD-BLYP yields a spheroidal shell structure

composed of nine 6-member rings, one 5- and one 3-member ring, plus two 10-member rings between which the central atom has bonded, with at least one C≡C bond (1.26 Å) and two C=C bonds (~1.36 Å) present; the overall structure is ~sp<sup>2</sup> with most bond lengths in the 1.41–1.49 Å range.

Octa6 × 6. Using VASP on C<sub>84</sub> crystal, Barnard et al.<sup>37</sup> report that the 74 surface atoms separate from the 10 inner core atoms with the outer carbon shell containing entirely sp<sup>2</sup> bonded atoms (C–C bond lengths ~1.45 Å), the inner core contracting to ~1.41 Å C–C bond lengths, with a shell–core separation distance of ~2.25 Å<sup>37</sup> or ~3 Å.<sup>19</sup> Using CPMD-PBE, CPMD-BLYP, and PRIRODA-PBE, we confirm that Octa6 × 6 acquires a round shape and separates from an inner core (Fig. 3(I); core atoms shown in

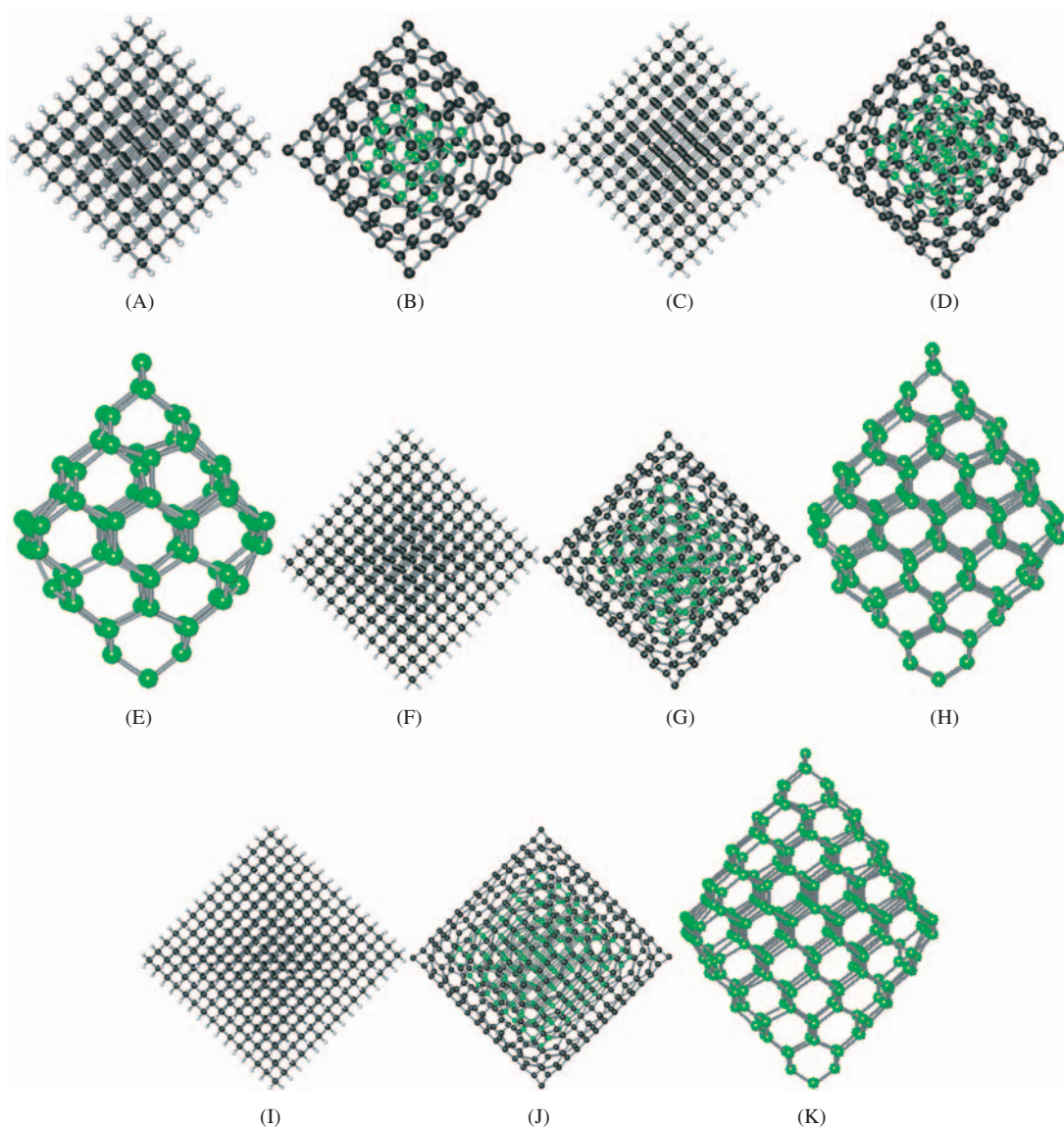


**Fig. 4.** Octahedron, side views: (A) Octa8 × 8H (PBE), (B) Octa8 × 8 (PBE), (C) Octa10 × 10H (PBE), (D) Octa10 × 10 (PBE), (E) core of Octa10 × 10, (F) Octa12 × 12H (PBE), (G) Octa12 × 12 (PBE), (H) core of Octa12 × 12, (I) Octa14 × 14H (PBE), (J) Octa14 × 14 (PBE), and (K) core of Octa14 × 14. (C = black, H = white, Core C Atoms = green).

green) that includes highly strained and pyramidalized C atoms (not a tetrahedral  $sp^3$  structure), with a shell–core separation distance of  $\sim 2.7$  Å.

Octa $8 \times 8$ H (Fig. 4(A)), Octa $10 \times 10$ H (Fig. 4(C)), Octa $12 \times 12$ H (Fig. 4(F)), Octa $14 \times 14$ H (Fig. 4(I)). CPMD-PBE predicts no reconstruction; all retain the original cleaved diamond structure with no graphitization of C(111) surfaces and no significant change in the length of surface or interior bonds.

Octa $8 \times 8$ . CPMD-PBE shows this structure optimizes to OLC with 130 fullerenic ( $sp^2$ ) outer shell atoms and 35 inner-shell core atoms with a partially  $sp^3$  bonding pattern, all with bondlengths in the 1.41–1.50 Å range and a shell–core separation distance of  $\sim 2.7$  Å (Fig. 4(B); core atoms shown in green). Barnard et al.<sup>37</sup> found a similar octahedral carbon-onion structure with a shell–core separation distance of  $\sim 2.25$  Å, using DFT(VASP) on  $C_{165}$  crystal. CPMD-PBE optimization yielded a few 3-member rings in both Octa $8 \times 8$  and Octa $6 \times 6$  structures; DFT(VASP)<sup>41</sup> also found 3-member rings on the reconstructed C(111)

surfaces of the similar-sized dehydrogenated octahedral diamond nanowires  $C_{108}$ ,  $C_{186}$  and  $C_{294}$ .

Octa $10 \times 10$ . Reconstructs to bucky-diamond (Fig. 4(D)) with a 202-atom  $sp^2$  fullerenic outer shell, surrounding an 84-atom  $sp^3$  diamondlike inner core (Fig. 4(E)) having highly compressed bonds.

Octa $12 \times 12$ . Reconstructs to bucky-diamond (Fig. 4(G)) with a 290-atom  $sp^2$  fullerenic outer shell, surrounding a 165-atom  $sp^3$  diamondlike inner core (Fig. 4(H)) having highly compressed bonds.

Octa $14 \times 14$ . Reconstructs to bucky-diamond (Fig. 4(J)) with a 397-atom  $sp^2$  fullerenic outer shell, surrounding a 283-atom  $sp^3$  diamondlike inner core (Fig. 4(K)) having highly compressed bonds. Using a less-computationally intensive density functional based tight binding method with self-consistent charges (SCC-DFTB), Barnard and Sternberg<sup>32</sup> also found that the core  $sp^3$  region continues to grow in size relative to the  $sp^2$  outer shell for the  $C_{969}$  (Octa $16 \times 16$ ),  $C_{1330}$  (Octa $18 \times 18$ ), and  $C_{1771}$  (Octa $20 \times 20$ ) nanodiamond octahedrons.

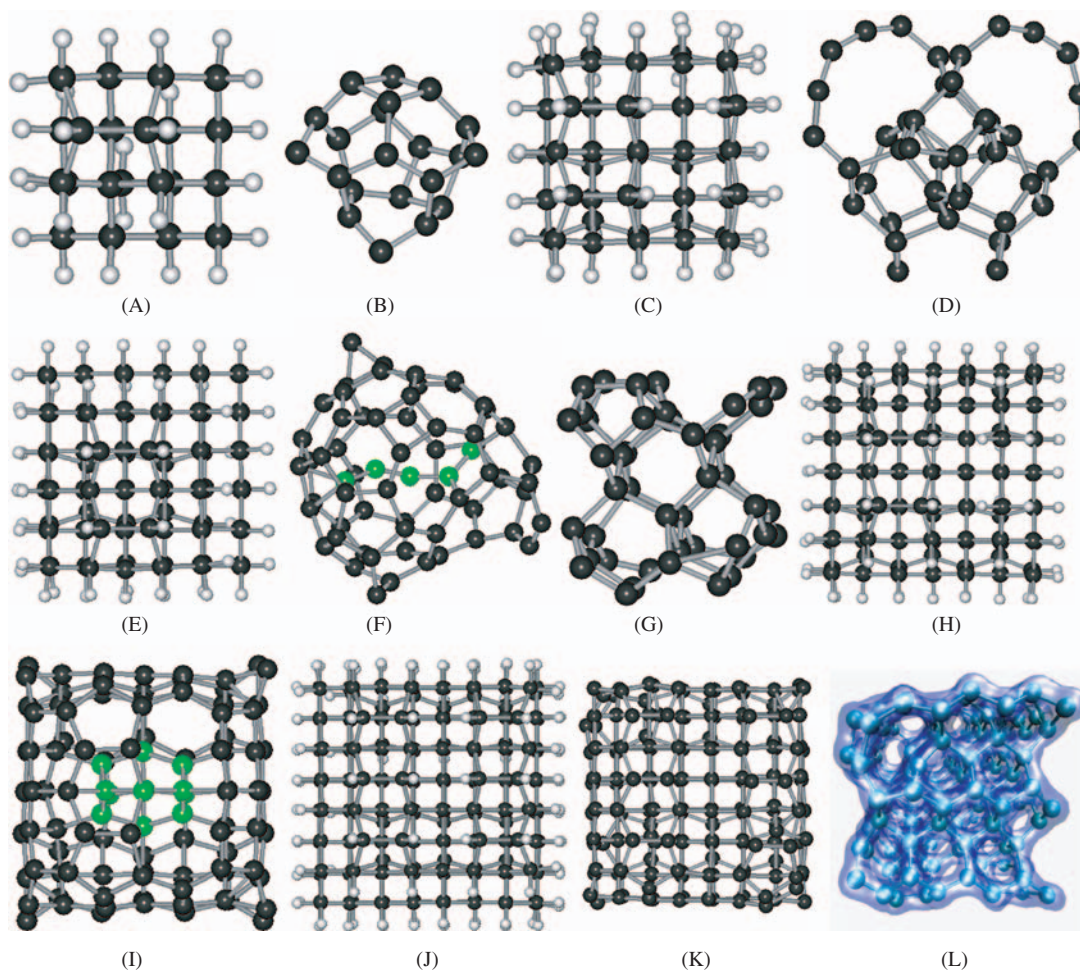


**Fig. 5.** Cuboid, top views: (A) Cube $3 \times 3$ H (PBE), (B) Cube $3 \times 3$  (PBE), (C) Cube $4 \times 4$ H (PBE), (D) Cube $4 \times 4$  (PBE), (E) Cube $5 \times 5$ H (PBE), (F) Cube $5 \times 5$  (PBE), (G) Cube $5 \times 5$  (MP2), (H) Cube $6 \times 6$ H (PBE), (I) Cube $6 \times 6$  (PBE), (J) Cube $7 \times 7$ H (PBE), (K) Cube $7 \times 7$  (PBE), and (L) Cube $7 \times 7$  electron density image (side view). (A–K: C = black, H = white, Core C Atoms = green).

### 3.2. Clean and Hydrogenated Nanodiamond Cuboids

Geometry optimizations of the cuboid nanodiamonds yielded the following results:

Cube $3 \times 3$ H. Does not reconstruct (all methods) (Fig. 5(A)). The dimerization on the C(100) faces in this and all subsequent hydrogenated cuboids is the only divergence from the regular tessellation pattern of  $sp^3$  carbon atoms in the lattice.

Cube $3 \times 3$ . CPMD-PBE optimized structure reconstructs into an  $sp^2$ -hybridized structure (possibly metastable) that includes two 4-carbon rings, two 5-carbon rings, and six 6-carbon rings with no endohedral atoms (Fig. 5(B)). Barnard<sup>19</sup> reported that a slightly larger  $C_{28}$  cuboid decayed to a “tetrahedral amorphous structure” that must be metastable, since the fullerene  $C_{28}$  is known to be the global energy minimum.

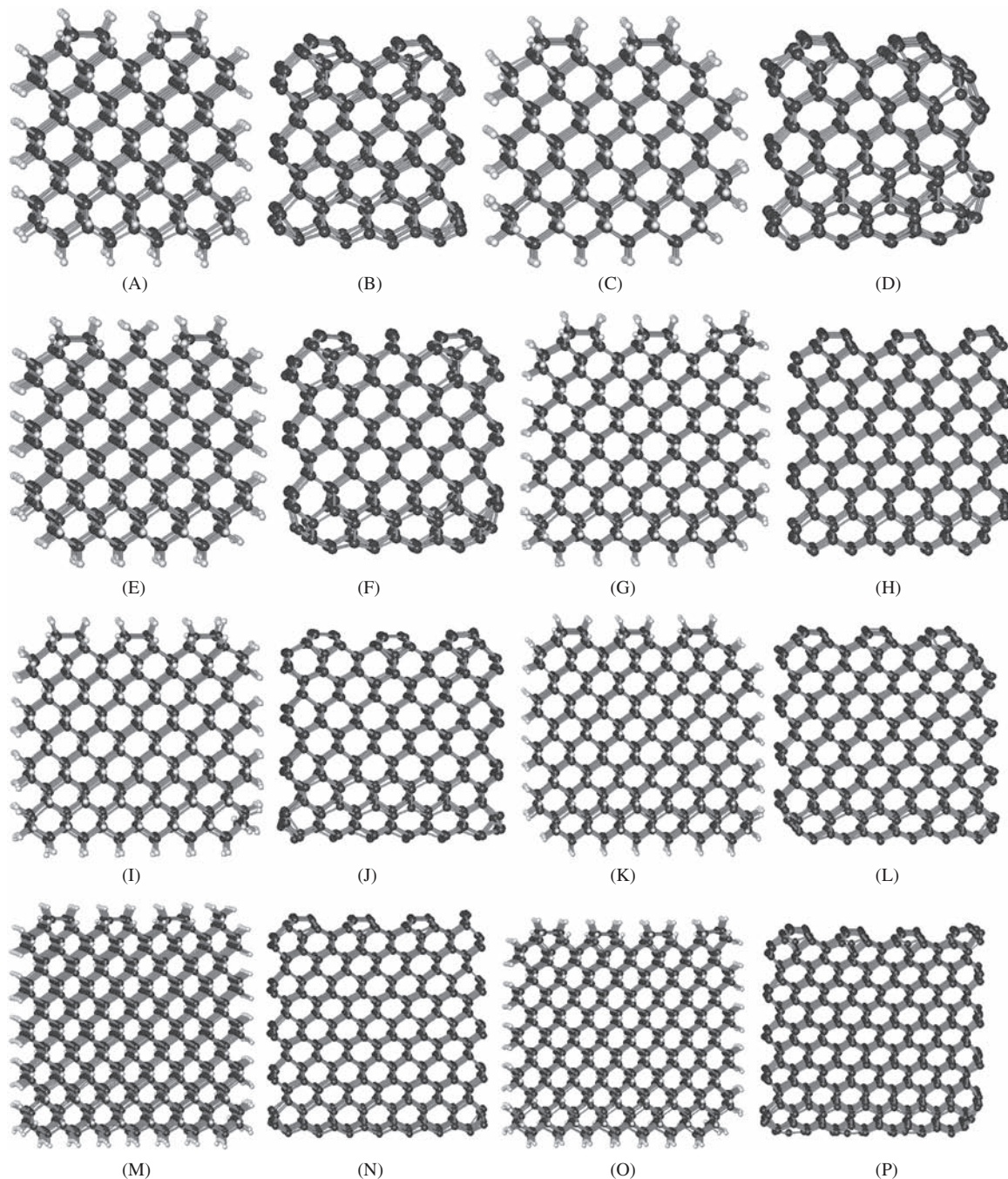


**Fig. 6.** Cuboid (all PBE), side views: (A) Cube $8 \times 8$ H, (B) Cube $8 \times 8$ , (C) Cube $9 \times 9$ H, (D) Cube $9 \times 9$ , (E) Cube $10 \times 10$ H, (F) Cube $10 \times 10$ , (G) Cube $11 \times 11$ H, (H) Cube $11 \times 11$ , (I) Cube $12 \times 12$ H, (J) Cube $12 \times 12$ , (K) Cube $13 \times 13$ H, (L) Cube $13 \times 13$ , (M) Cube $14 \times 14$ H, (N) Cube $14 \times 14$ , (O) Cube $15 \times 15$ H, and (P) Cube $15 \times 15$ . (C = black, H = white).

Cube4 × 4H (Fig. 5(C)), Cube5 × 5H (Fig. 5(E)), Cube6 × 6H (Fig. 5(H)), Cube7 × 7H (Fig. 5(J)). Does not reconstruct (all methods).

Cube4 × 4. CPMD-PBE optimized structure reconstructs into an sp<sup>2</sup>-hybridized structure (likely only metastable) that includes a 10- and a 12-carbon-chain loop reminiscent of cumulene rearrangement intermediates often seen in the self-assembly of small fullerenes (Fig. 5(D)).

Cube5 × 5. CPMD-PBE optimized structure reconstructs into a fullerene spheroidal shell, which is separated from an inner core of 5 atoms (Fig. 5(F); core atoms shown in green) two of which are bonded at an ethynyl-like bondlength (1.215 Å) and bonded at either end to neighboring carbon atoms through ethenyl-like bondlengths (~1.36 Å). It is likely that this is only a metastable local energy minimum but we have not investigated the structure further. The PRIRODA-MP2 geometry (Fig. 5(G)) is a highly distorted sp<sup>3</sup> lattice that appears transitional because many C–C bondlengths are fullerene and the geometry includes at least four 1.21–1.24 Å C≡C structures.

Cube6 × 6. CPMD-PBE optimized structure retains some sp<sup>3</sup> bonding connectivity but the outer shell appears mostly fullerene (Fig. 5(I)), and two internal voids have opened inside two neighboring corners due to the near-pyramidalization of two carbon atoms in an endohedral 3-member ring (producing some 9- and 10-member rings). There is 3- and 4-member ring formation both internally and in the outer shell. This may be a transitional structure on the path to graphitization.

Cube7 × 7. CPMD-PBE optimized structure retains mostly sp<sup>3</sup> bonding connectivity (Fig. 5(K)), though many bonds between core and shell region are highly strained bonds (and a few of them are broken) and one internal void has opened up near one corner (visible at upper left in the electron density isosurface image of Cube7 × 7) (Fig. 5(L)).

Cube8 × 8H (Fig. 6(A)), Cube9 × 9H (Fig. 6(C)), Cube10 × 10H (Fig. 6(E)), Cube11 × 11H (Fig. 6(G)), Cube12 × 12H (Fig. 6(I)), Cube13 × 13H (Fig. 6(K)), Cube14 × 14H (Fig. 6(M)), Cube15 × 15H (Fig. 6(O)). CPMD-PBE predicts no reconstruction; all retain the original cleaved diamond structure with no graphitization of C(111) surfaces and no significant change in the length of surface or interior bonds.

Cube8 × 8 (Fig. 6(B)), Cube9 × 9 (Fig. 6(D)), Cube10 × 10 (Fig. 6(F)), Cube11 × 11 (Fig. 6(H)), Cube12 × 12 (Fig. 6(J)), Cube13 × 13 (Fig. 6(L)), Cube14 × 14 (Fig. 6(N)), Cube15 × 15 (Fig. 6(P)). CPMD-PBE optimized structures retain mostly sp<sup>3</sup> bonding connectivity, with most interior lattice bondlengths normal for diamond, bonds between core and outermost shell slightly to moderately stretched (1.56–1.68 Å), and bonds within the outermost shell somewhat compressed (1.42–1.52 Å). Using a less-computationally intensive density functional based

tight binding method with self-consistent charges (SCC-DFTB), Barnard and Sternberg<sup>32</sup> also found that the alternative nanodiamond cuboids C<sub>259</sub>, C<sub>712</sub>, C<sub>881</sub> and C<sub>1798</sub> are essentially all sp<sup>3</sup>-bonded except for a narrow line of atoms along the C(110)/C(110) edges which have sp<sup>2</sup> hybridization.

These results generally support Barnard's contention<sup>19</sup> that although there is preferential exfoliation of C(111) surfaces over lower index surfaces on isolated clusters, even fully dehydrogenated nanodiamonds up to 2 nm may be stable in the absence of C(111) surfaces. Our results, obtained for 0 K, are also consistent with findings by others<sup>85,86</sup> using DFTB at finite temperature on similar structures.

### 3.3. Dimerization Patterns on Nanodiamond C(100) Faces

For C(100) surfaces on cuboids with an odd number of north-south dimerizable rows (Cube6 × 6H, Cube10 × 10H,

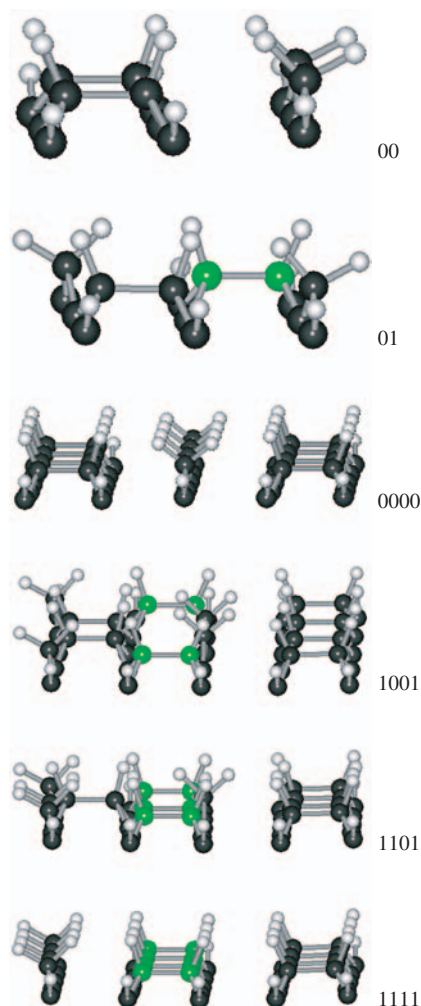


**Fig. 7.** Representative dimerization patterns on cuboid C(100) faces for Cube6 × H(–00, –01) and Cube10 × 10H(–0000, –1001, –1101, –1111). (C = black, H = white, shifted dimer = green).

**Table II.** Geometry-optimized relative energies for dimerization patterns on C(100) faces of the 1.5-nm cuboid nanodiamond C<sub>428</sub>H<sub>200</sub> (Cube10 × 10H).

Dimerization pattern	Relative energy (eV)	Dimerization pattern	Relative energy (eV)
0000	+0.13	1001	+3.83
1000 (=0001)	+3.80	0110	+4.70
0100 (=0010)	+4.40	1110 (=0111)	+4.87
1100 (=0011)	+4.47	1101 (=1011)	+3.48
1010 (=0101)	+5.30	1111	0.00

and Cube14 × 14H), one north-south row will be unpaired, creating a variety of possible dimerization patterns (Fig. 7). Cube6 × 6H-00 is −0.33 eV lower in energy than Cube6 × 6H-01 and Cube6 × 6-00 is −3.32 eV lower in energy than Cube6 × 6-01. For dimerization patterns on a C(100) face on Cube10 × 10H, the 0000 pattern with the solitaire row between two dimer rows is +0.13 eV higher in energy than the 1111 pattern with the solitaire row nearest the face edge, which appears to be the global minimum. The mixed-row patterns 1001 and 1101 are +3.83 eV and +3.48 eV higher in energy, respectively, than 1111. The relative energies for all ten dimerization patterns (Table II) suggest that parallel rows of dimers and solitaires are significantly preferred to mixed rows containing both dimers and solitaires (mixed dimer positions increase structural tension). Additionally, solitaire rows placed nearest the edge of a face are slightly preferred to solitaire rows in internal positions.

### 3.4. Partial Dehydrogenation of Nanodiamond Surfaces

In order to extend a structure using DMS, one or more neighboring radical sites must be created on a growing passivated nanodiamond workpiece that is elsewhere completely passivated. These sites exist either after removing one or more H atoms using a positionally-controlled hydrogen abstraction tool or after failing to passivate an existing radical site using a positionally-controlled hydrogen donation tool. To address the question of how many adjacent radical sites may be simultaneously present on a nanodiamond facet before the underlying sp<sup>3</sup> lattice begins to reconstruct, multiple neighboring H atoms were removed in specific patterns from representative mid-facet, edge, and vertex locations on a C(111)–H(1 × 1) face (the most graphitization-prone diamond surface) of the octahedron nanodiamond Octa12 × 12H.

In a first series of calculations, hydrogen atoms were removed in progressively larger numbers from C(111) octahedral mid-facet positions. The removal of the first H atom from lattice surface atom C203 (Fig. 8(A)) causes this carbon atom to drop slightly lower into the lattice, its three supporting C–C bondlengths decreasing from 1.540 Å to 1.50 Å. The removal of a second H atom from lattice

surface atom C327 at the 4 o'clock position relative to C203 (Fig. 8(B)) causes both C atoms to drop slightly more, with the C–C bond to their one mutual subsurface neighbor C atom decreasing to 1.473 Å and their C–C bonds to their two non-mutual subsurface neighbor C atoms falling to 1.501 Å and 1.491 Å, respectively; removing the second H atom from lattice surface atom C205 at the 2 o'clock position (Fig. 8(C)) yields similar bondlengths. Removing the second H atom from lattice surface atom C306 at the 8 o'clock position (Fig. 8(D)) causes the six C–C lattice bonds to the two depassivated C atoms to compress slightly to 1.494 Å but all neighboring bonds remain unchanged near 1.540 Å. Removal of 3H atoms in a triangle pattern from C203, C205, and C317 (which lies at 3 o'clock relative to C203) (Fig. 8(E)) yields C–C bondlengths to the mutual subsurface C atom of 1.501 Å; for interior atom C205 the other two C–C bondlengths are 1.501 Å and 1.502 Å, whereas for the endmost atoms C203 and C317 the other two C–C bondlengths are 1.503 Å and 1.506 Å. There are only negligible changes in the in-plane C–C bondlengths immediately peripheral to the C203–C205–C317 triad, but one isolated cross-plane C–C bond between atoms C204 and C206 (below C205) moderately stretches to 1.658 Å.

Removing 4H atoms in a “parallelogram” pattern from carbon atoms C203, C205, C317 and C235 (Fig. 8(F)) causes more significant lattice distortion. (The same atoms appear as a “square” pattern when camera position is moved to a different vertex; Fig. 8(G)) The C–C bondlength to the mutual subsurface C atom (C204) shared by 3 dehydrogenated C atoms averages 1.475 Å with in-plane bond angles increasing from the relaxed tetrahedral 109.5° to a slightly strained 118°. The C–C bondlengths to the mutual subsurface C atom (C318) shared by 2 dehydrogenated C atoms average 1.477 Å. The seven remaining C–C bondlengths between the four dehydrogenated C atoms and their neighboring subsurface C atoms average 1.497 ± 0.005 Å. The in-plane C–C bondlengths immediately peripheral to the parallelogram are largely unchanged; immediately underneath the dehydrogenated pattern the cross-plane C–C bondlengths are modestly stretched, in the 1.55–1.59 Å range, but this cross-plane strain is largely absent from the next-deepest layer under the pattern. However, the cross-plane bond between C318 and C322 (below C235) is stretched to 1.701 Å and the cross-plane bond between C204 and C206 (below C205) is highly stretched to 1.823 Å (close to the 1.87 Å Morse bond scission distance for C–C), indicating incipient rearrangement near the two mutually shared C204 and C318 atoms.

Removing 4H atoms in a 3-in-line pattern from atoms C214, C203, C317 and C205 (Fig. 8(H)) produces similar significant lattice distortion. The C–C bondlength to the mutual subsurface C atom (C204) shared by 3 dehydrogenated C atoms averages 1.469 Å with in-plane bond angles again increasing to a slightly strained 119°. The

C–C bondlengths to the mutual subsurface C atom (C227) shared by 2 dehydrogenated C atoms average  $1.470 \text{ \AA}$ . The seven remaining C–C bondlengths between the four dehydrogenated C atoms and their neighboring subsurface C atoms average  $1.500 \pm 0.004 \text{ \AA}$ . The in-plane C–C bondlengths immediately peripheral to the parallelogram are largely unchanged; immediately underneath the dehydrogenated pattern the cross-plane C–C bondlengths are modestly stretched, in the  $1.55\text{--}1.59 \text{ \AA}$  range. However, the cross-plane bond between C227 and C228 (below C214) is stretched to  $1.735 \text{ \AA}$  and the cross-plane bond between C204 and C206 (below C203) is stretched to  $1.849 \text{ \AA}$  (close to the  $1.87 \text{ \AA}$  Morse bond scission distance for C–C), again indicating incipient rearrangement.

Increasing the number of neighboring dehydrogenations to 5H atoms (Fig. 8(I)) produces an optimized structure very similar to the 4-atom removal pattern shown in Figure 8(F) but apparently lacking high-strain C–C bondlengths exceeding  $1.634 \text{ \AA}$ . A short (24 fs) MD simulation at 300 K yields no rearrangements of this structure.

The surface transformation to “onion-like” geometry may involve changing the conformation from “concave” to “convex” for surface fragment carbon atoms possessing interlayer bonds, in which case the complete reconstruction of a surface fragment probably requires passing through a number of intermediate states. For instance, in a calculation started from one such possible intermediate state in which the C204–C206 distance is initialized at  $3 \text{ \AA}$  ( $\sim$  double the normal C–C bondlength), atom C206 remains in the “convex” geometry after structure optimization, during which the C204–C206 distance stabilizes at  $2.403 \text{ \AA}$  (well above the normal  $1.54 \text{ \AA}$  C–C bondlength, indicating a broken bond), yielding an intermediate “graphitized” state that lies  $0.43 \text{ eV}$  higher in energy than the optimized structure shown in Figure 8(I). However, a complete analysis of intermediate states that lead to graphitization is beyond the scope of this work.

In a second series of calculations, hydrogen atoms were removed in progressively larger numbers along C(111) octahedral edge positions. The removal of the first H atom

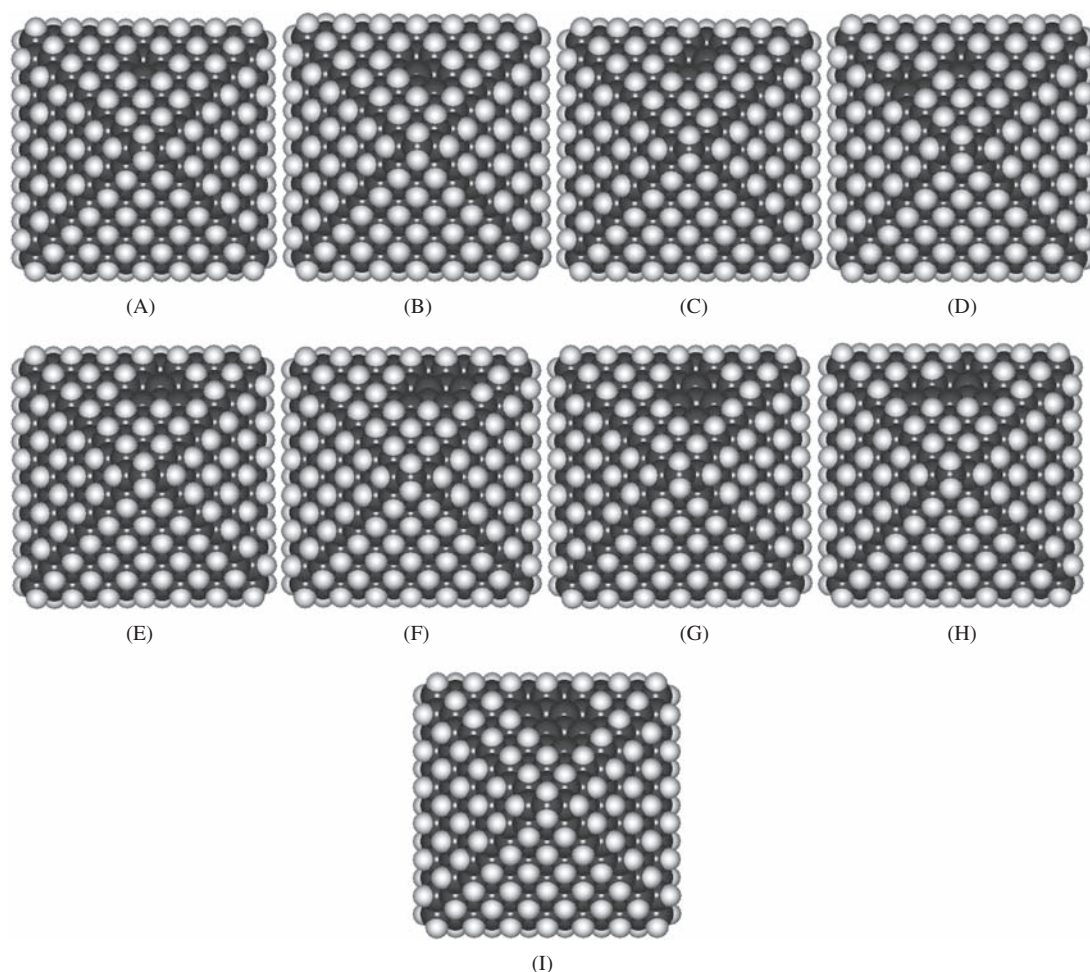


**Fig. 8.** Removal of H atoms from mid-facet positions on C(111)–H-(1 × 1) face of Octa12 × 12H (top view, 2.3 nm edge length, init. 651 atoms): removed 1 atom (A); 2 atoms in line toward edge (B), parallel to edge (C), or separated by one row (D); 3 atoms nearest-neighbor (E); 4 atoms nearest-neighbor parallelogram (F), nearest-neighbor square (G), or 3-in-line (H); and 5 atoms nearest-neighbor (I). (C = black, H = white).

from lattice surface atom C216 (Fig. 9(A)) causes the carbon atom to drop slightly lower into the lattice, its three C–C bondlengths decreasing from 1.540 Å to 1.500 Å.

The removal of a second H atom from lattice surface atom C211 along the edgeline (Fig. 9(B)) causes both C216 and C211 to drop slightly more, with the C–C bondlengths to their one mutual subsurface neighbor C atom decreasing to 1.465 Å, the C–C bondlengths to their two non-mutual subsurface neighbor C atoms falling to 1.493 Å, and the cross-plane bonds below atoms C216 and C211 stretching slightly to 1.57 Å. Removing the second H atom from lattice surface atom C205 above the edge (Fig. 9(C)) yields similar bondlength changes (mutual bondlengths to atom C218 at 1.472 Å, nonmutual bondlengths 1.491 Å), but one isolated cross-plane C–C bond between atoms C218 and C219 (below C216) stretches to 1.724 Å. Removing the second H atom from lattice surface atom C217 below the edge (Fig. 9(D)) allows a 1.384 Å C=C bond to form between C216 and C217 as typically happens when two mutually-bonded C atoms are both dehydrogenated.

The C=C dimer drops just slightly into the lattice as the four C–C bonds supporting either end of the dimer decline in length to 1.51 Å, while the cross-plane C–C bonds between atoms C218 and C219 (below C216) and between atoms C220 and C221 (below C217) stretch moderately to 1.622 Å.

The removal of a third H atom from lattice surface atom C18 along the edgeline defined by C216 and C211 (Fig. 9(E)) causes all three dehydrogenated C atoms to drop slightly into the lattice, with the C–C bondlengths to their three lattice support atoms decreasing to an average 1.500 Å (C211), 1.498 Å (C216) and 1.500 Å (C18), and the three cross-plane C–C bonds underneath each of the three dehydrogenated atoms stretching slightly to an average 1.576 Å. Removing H atoms from C205, C216 and C226 with two C atoms above the edge (Fig. 9(F)) gives a triangle pattern similar to Figure 8(D), with C–C bondlengths to the mutual subsurface C atom (C218) of 1.502 Å, bondlengths to the nonmutual support atoms of 1.500 Å, negligible changes in the in-plane C–C bondlengths immediately peripheral

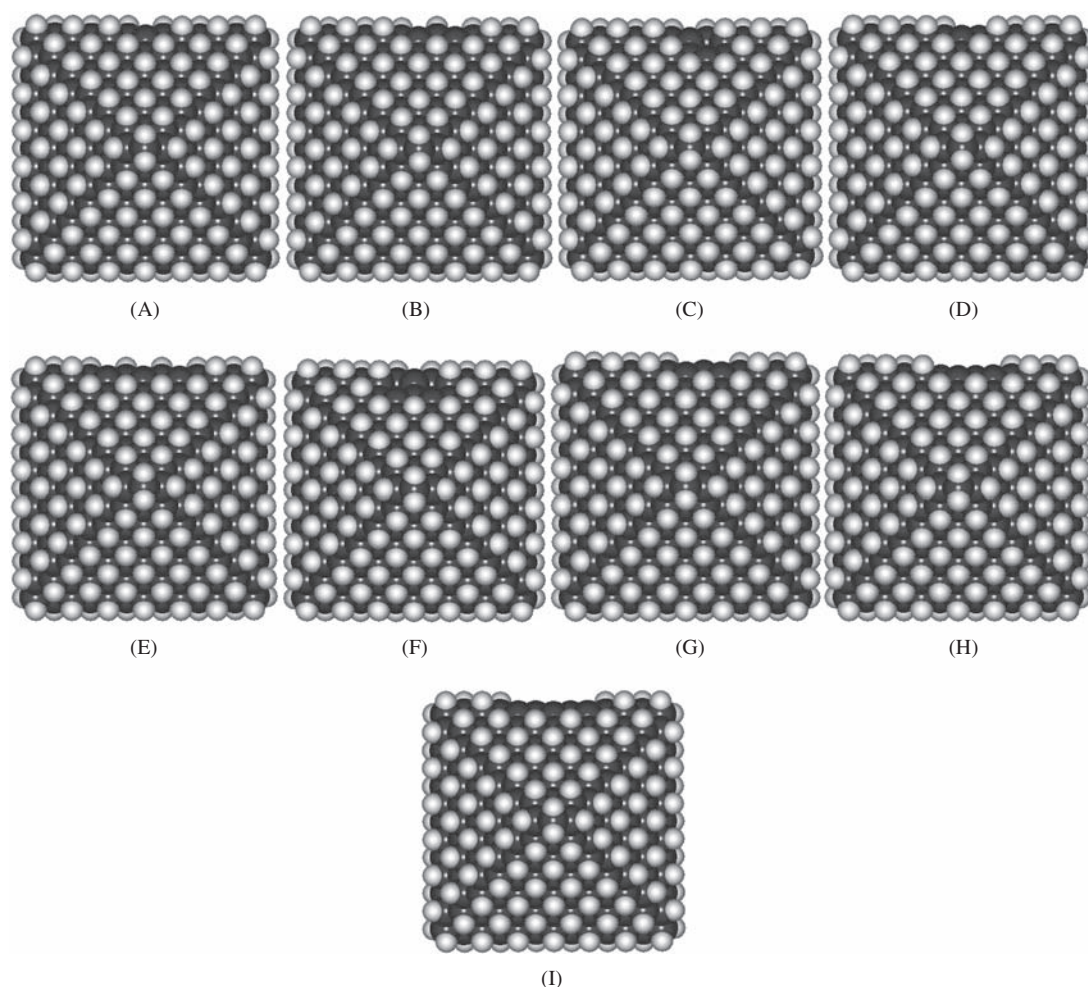


**Fig. 9.** Removal of H atoms from edge positions along C(111)–H-(1 × 1) face of Octa12 × 12H (top view, 2.3 nm edge length, init. 651 atoms): removed 1 edge atom (A); 2 atoms in line along edge (B) 1 above edge (C), or 1 below edge (D); 3 atoms, in line along edge (E) 2 above edge (F), or 1 below edge (G); 4 atoms, 2 in line along edge and 2 below edge (H); and 5 atoms, 3 in line along edge and 2 below edge (I). (C = black, H = white).

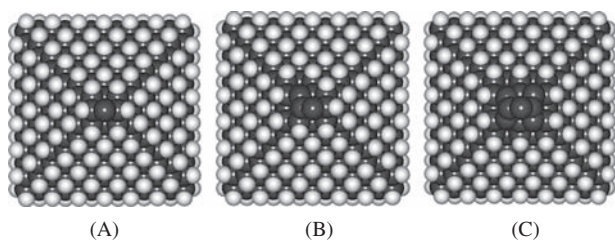


**Fig. 10.** Removal of H atoms from vertex junction of four C(111)-H-(1 × 1) faces of Octa12 × 12H (top view, 2.3 nm edge length, init. 651 atoms): removed 2 atoms from apical C atom (A); 4 atoms, 2 from apical C atom and 2 from two side C atoms (B); and 8 atoms, 2 from apical C atom and 6 from nearest-neighbor side C atoms (C). (C = black, H = white).

to the C<sub>205</sub>-C<sub>216</sub>-C<sub>326</sub> triad, and one isolated cross-plane C-C bond

between atoms C<sub>218</sub> and C<sub>219</sub> (below C<sub>216</sub>) moderately stretched to 1.659 Å. Removing H atoms from C<sub>216</sub>, C<sub>217</sub> and C<sub>211</sub> with one C atom below the edge (Fig. 9(G)) yields a line of three dehydrogenated mutually-bonded C atoms with 1.424 Å bondlengths; the local structure apparently adopts sp<sup>2</sup> hybridization because the three C atoms are unable to form two adjacent C=C bonds. Atoms C<sub>216</sub> and C<sub>211</sub> have 1.504 Å bonds to two C atoms at either end; center atom C<sub>217</sub> has a 1.577 Å bond to the C atom beneath it, which in turn has two 1.522 Å C-C bonds and one modestly stretched 1.597 Å bond to its three neighboring C atoms, but there are no other lattice distortions of significance.

Removing four H atoms from C<sub>19</sub>, C<sub>216</sub>, C<sub>217</sub> and C<sub>211</sub> with two C atoms below the edge (Fig. 9(H)) yields a chain of four dehydrogenated C atoms, with two pairs double-bonded as -C=C-C=C- having interior bondlengths 1.394 Å, 1.451 Å, and 1.395 Å, respectively. (The singlet lies -0.80 eV below the triplet multiplicity for this structure.) There are also two C-C bonds directly beneath C<sub>19</sub> and C<sub>217</sub> in the C(111) cross-plane direction that are stretched to an average 1.622 Å, indicating a growing potential for graphitization, but the cross-plane stretched region is still too small to seriously deform the lattice.

Removing five H atoms from C<sub>18</sub>, C<sub>19</sub>, C<sub>216</sub>, C<sub>217</sub> and C<sub>211</sub> with two C atoms below the edge (Fig. 9(I)) yields a chain of five dehydrogenated C atoms with average C-C bondlengths 1.425 Å (vs. 1.545 Å for neighboring C-C bonds), cross-plane bondlengths averaging 1.507 Å (vs. 1.546 Å) to the second layer and two cross-plane bondlengths stretched to 1.629 Å to the third layer, but still no evidence for outright graphitization.

In a third series of calculations, hydrogen atoms were removed in progressively larger numbers from C(111) octahedral vertex positions. Removing both H atoms from the apical carbon atom C<sub>429</sub> (Fig. 10(A)) reduces bondlength to its two lattice C atoms (C<sub>455</sub>, C<sub>428</sub>) to an average 1.487 Å, and the bonds to the four C atoms (C<sub>313</sub>, C<sub>454</sub>, C<sub>422</sub>, C<sub>430</sub>) below C<sub>455</sub> and C<sub>428</sub> stretch very slightly to 1.566 Å. Removing four H atoms, two from the apical C<sub>429</sub> and one each from carbon atoms C<sub>455</sub> and C<sub>313</sub> immediately below C<sub>429</sub> (Fig. 10(B)) produces compressed

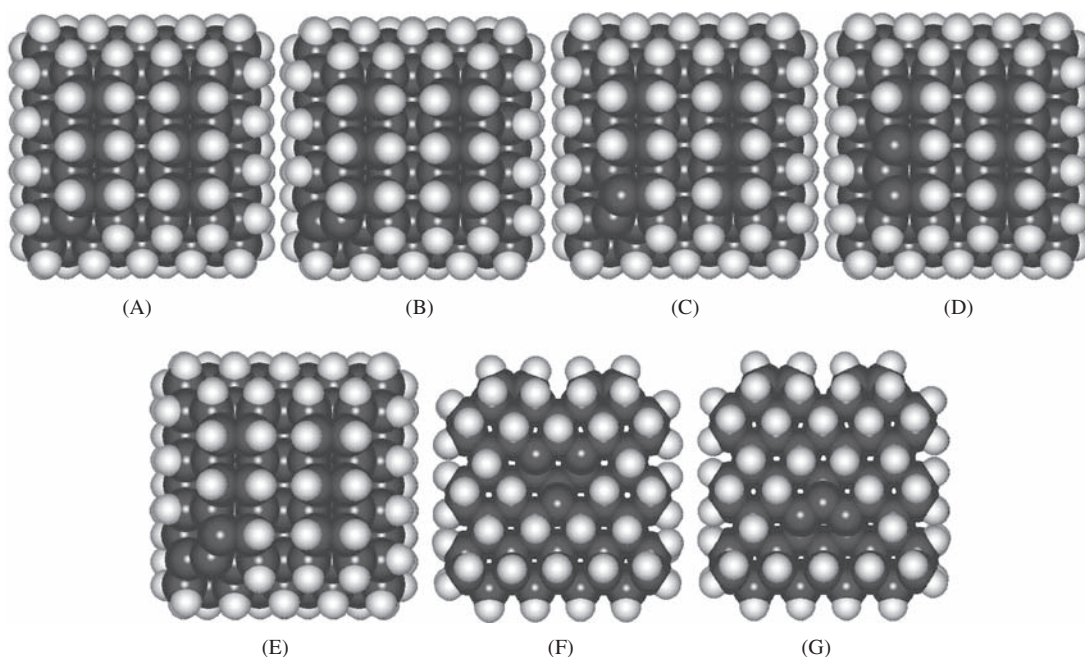


**Fig. 11.** Removal of H atoms from locations along a C(100)-H-(1 × 1)/C(110)-H-(1 × 1) edge of Cube8 × 8H (top view of C(100), 1.2 nm edge length, init. 380 atoms): removed 1 atom, south edge (A); 2 atoms, south edge and west edge (B), south edge and north-south row (C), or same north-south row (D); 3 atoms, south edge, west edge and north-south row (E). Also, removal of H atoms from locations on a C(110)-H-(1 × 1) face of Cube8 × 8H: 3 atoms removed along a trough (F), 3 atoms removed along a ridge (G). (C = black, H = white).

1.406 Å bonds between C<sub>429</sub>–C<sub>455</sub> and C<sub>455</sub>–C<sub>313</sub>, and a moderately stretched 1.604 Å bond between C<sub>428</sub>–C<sub>430</sub>. Removing four more H atoms from the next lowest four C atoms, for a total of 8H atom removals (Fig. 10(C)), produces an asymmetric tip with 1.411 Å (C<sub>429</sub>–C<sub>428</sub>) and 1.488 Å (C<sub>429</sub>–C<sub>455</sub>) C–C bonds to apical atom C<sub>429</sub>. The two C–C bonds beneath C<sub>428</sub> average 1.458 Å below which the next four C–C lattice bonds average 1.512 Å, and the two C–C bonds beneath C<sub>455</sub> average 1.413 Å below which the next four C–C lattice bonds average 1.528 Å. Between the 4th and 5th planes, atom C<sub>316</sub> which lies directly below C<sub>429</sub> in the lattice framework has two C–C bonds stretched to 1.624 Å, but all other bonds in the lattice appear near the 1.540 Å average and the entire lattice geometry remains intact.

In a fourth set of calculations, one (Fig. 11(A)), two (Fig. 11(B), Fig. 11(C), Fig. 11(D)) and three (Fig. 11(E)) H atoms were removed from locations along a C(100)–H(1 × 1)/C(110)–H(1 × 1) edge of the cuboid nanodiamond Cube8 × 8H. Bondlengths between dehydrogenated C atoms decreased to the 1.39–1.45 Å range but the lattice geometry was not disrupted.

There is no evidence or suggestion in the experimental or theoretical literature that the structure of the C(110)–H(1 × 1) surfaces of a cuboid nanodiamond might be changed by altering the surface passivation pattern. Nevertheless, one last set of calculations was performed in which three H atoms were removed from a C(110)–H(1 × 1) surface along a trough (Fig. 11(F)) where there is no possibility of change in bond order (C–C bondlengths to dehydrogenated atoms along ridge contract only slightly to 1.47–1.50 Å; one C–C bond from the CH between the two dehydrogenated ridge carbons, down into the lattice, stretches to 1.639 Å), and along a ridge (Fig. 11(G)) where a change in bond order (to pi chain) is expected and is observed (C–C bondlengths along ridge: 1.550 Å–1.509 Å–1.426 Å–1.427 Å–1.509 Å–1.551 Å; dehydrogenated atom bondlengths down into the lattice decline slightly from 1.553 Å to 1.512 Å). No pathological reconstructions were observed in either case.

## 4. CONCLUSIONS

Computational studies using Density Functional Theory (DFT) have determined that fully hydrogenated nanodiamonds up to 2 nm (~900–1800 atoms) in size having only C(111) faces (octahedrons) or only C(110) and C(100) faces (cuboids) maintain stable sp<sup>3</sup> hybridization. Fully dehydrogenated cuboid nanodiamonds above 1 nm retain the diamond lattice pattern, but smaller dehydrogenated cuboids and dehydrogenated octahedron nanodiamonds up to 2 nm reconstruct to bucky-diamond or onion-like carbon (OLC). Up to three adjacent passivating H atoms may be removed from mid-facet locations on the most

graphitization-prone C(111) face of an octahedron nanodiamond without reconstruction of the underlying diamond lattice; removal of a fourth or fifth H atom increases 1–2 cross-plane bondlengths indicating incipient graphitization. H atom removals from an even number of adjacent mutually-bonded C atoms along octahedral edges will form C=C bonds; aside from this change in bond order, up to five H removals along edges will moderately stretch 1–2 cross-plane bondlengths but will not disrupt the octahedron diamond lattice. Removing up to 8H atoms from vertex locations on a nanodiamond octahedron, and H removals from C(100) or C(110) surfaces in compact patterns, also produce no lattice reconstructions. On C(100) surfaces of cuboid nanodiamonds, parallel rows of carbon dimers and solitaires are energetically preferred to mixed rows containing both dimers and solitaires, and solitaire rows placed nearest the edge of a face are slightly preferred to solitaire rows located at interior positions on the face.

We conclude that fully- and mostly-H-passivated simple cuboid and octahedral diamond nanoparts possess at least static structural stability. These results support the conservative DMS fabrication strategy outlined in Freitas and Merkle<sup>1</sup> wherein atomically precise diamond nanoparts are fabricated using reaction sequences that minimize the number of exposed surface radicals during any intermediate phase of a mechanosynthetic operation, and wherein all surfaces are kept fully hydrogenated at all times during fabrication except for single-site dehydrogenations that are required to complete an addition or attachment (e.g., ring closing) operation.

**Acknowledgments:** The authors acknowledge comments on an earlier version of the manuscript by Amanda S. Barnard and graphics assistance by Damian G. Allis. Robert A. Freitas, acknowledges private grant support for this work from the Life Extension Foundation, the Kurzweil Foundation, and the Institute for Molecular Manufacturing.

## References

1. R. A. Freitas, Jr. and R. C. Merkle, *J. Comput. Theor. Nanosci.* 5, 760 (2008).
2. D. Tarasov, N. Akberova, E. Izotova, D. Alisheva, M. Astafiev, and R. A. Freitas, Jr., *J. Comput. Theor. Nanosci.* 7, 325 (2010).
3. D. M. Eigler and E. K. Schweizer, *Nature* 344, 524 (1990).
4. N. Oyabu, O. Custance, I. Yi, Y. Sugawara, and S. Morita, *Phys. Rev. Lett.* 90, 176102 (2003).
5. N. Oyabu, O. Custance, M. Abe, and S. Moritabe, Abstracts of Seventh International Conference on Non-Contact Atomic Force Microscopy, Seattle, Washington, USA, September (2004), p. 34.
6. Y. Sugimoto, P. Pou, O. Custance, P. Jelinek, M. Abe, R. Perez, and S. Morita, *Science* 322, 413 (2008).
7. R. E. Tuzun, D. W. Noid, and B. G. Sumpter, *J. Chem. Phys.* 105, 5494 (1996).
8. K. Sohlberg, R. E. Tuzun, B. G. Sumpter, and D. W. Noid, *Nanotechnology* 8, 103 (1997).

9. D. W. Noid, R. E. Tuzun, and B. G. Sumpter, *Nanotechnology* 8, 119 (1997).
10. D. H. Robertson, B. I. Dunlap, D. W. Brenner, J. W. Mintmire, C. T. White et al., Novel forms of carbon II, *MRS Symposium Proceedings Series*, edited by C. L. Renschler, D. M. Cox, J. J. Pouch, and Y. Achiba (1994), Vol. 349, p. 283.
11. J. Han, A. Globus, R. Jaffe, and G. Deardorff, *Nanotechnology* 8, 95 (1997).
12. A. Globus, C. W. Bauschlicher, Jr., J. Han, R. L. Jaffe, C. Levit, and D. Srivastava, *Nanotechnology* 9, 192 (1998).
13. R. E. Tuzun, D. W. Noid, and B. G. Sumpter, *Nanotechnology* 6, 52 (1995).
14. O. A. Shenderova, D. Areshkin, and D. W. Brenner, *Mater. Res.* 6, 11 (2003).
15. K. E. Drexler, *Nanosystems: Molecular Machinery, Manufacturing, and Computation*, John Wiley & Sons, New York (1992).
16. T. Cagin, A. Jaramillo-Botero, G. Gao, and W. A. Goddard, III, *Nanotechnology* 9, 143 (1998).
17. G. Leach, *Nanotechnology* 7, 197 (1996).
18. J. C. Angus, A. Argoitia, R. Gat, Z. Li, M. Sunkara, L. Wang, and Y. Wang, *Phil. Trans. R. Soc. London A* 342, 195 (1993).
19. A. S. Barnard, O. A. Shenderova and D. M. Gruen (eds.), *Ultra Nanocrystalline Diamond: Synthesis, Properties and Applications*, William Andrew Publishing, New York (2006), p. 117.
20. F. Fugaciu, H. Hermann, and G. Seifert, *Phys. Rev. B* 60, 10711 (1999).
21. J. Y. Raty, G. Galli, C. Bostedt, T. W. van Buuren, and L. J. Terminello, *Phys. Rev. Lett.* 90, 37402 (2003).
22. A. S. Barnard, S. P. Russo, and I. K. Snook, *J. Chem. Phys.* 118, 5094 (2003).
23. L. T. Sun, J. L. Gong, Z. Y. Zhu, D. Z. Zhu, S. X. He, Z. X. Wang, Y. Chen, and G. Hu, *Appl. Phys. Lett.* 84, 2901 (2004).
24. M. Y. Gamarnik, *Nanostruct. Mater.* 7, 651 (1996).
25. M. Y. Gamarnik, *Phys. Rev. B* 54, 2150 (1996).
26. D. Zhao, M. Zhao, and Q. Jiang, *Diam. Relat. Mater.* 11, 234 (2002).
27. S. Praver, J. L. Peng, J. O. Orwa, J. C. McCallum, D. N. Jamieson, and L. A. Bursill, *Phys. Rev. B* 62, R16360 (2000).
28. N. W. Winter and F. H. Ree, *J. Comput.-Aided Mater. Des.* 5, 279 (1998).
29. F. H. Ree, N. W. Winter, J. N. Glosli, and J. A. Viecelli, *Physica B* 265, 223 (1999).
30. B. Wen, J. Zhao, and T. Li, *Chem. Phys. Lett.* 441, 318 (2007).
31. A. L. Verechshagin, *Combust. Exp. Shock Waves* 38, 358 (2002).
32. A. S. Barnard and M. Sternberg, *J. Mater. Chem.* 17, 4811 (2007).
33. O. A. Shenderova, V. V. Zhirnov, and D. W. Brenner, *Crit. Rev. Solid State Mater. Sci.* 27, 227 (2002).
34. N. Park, K. Lee, S. W. Han, J. J. Yu, and J. Ihm, *Phys. Rev. B* 65, 121405 (2002).
35. A. S. Barnard, S. P. Russo, and I. K. Snook, *Phys. Rev. B* 68, 073406 (2003).
36. V. L. Kuznetsov, I. L. Zilberberg, Y. V. Butenko, A. L. Chuvilin, and B. Seagall, *J. Appl. Phys.* 86, 863 (1999).
37. A. S. Barnard, S. P. Russo, and I. K. Snook, *Intl. J. Mod. Phys. B* 17, 3865 (2007).
38. S. P. Russo, A. S. Barnard, and I. K. Snook, *Surf. Rev. Lett.* 10, 233 (2003).
39. A. S. Barnard and I. K. Snook, *J. Chem. Phys.* 120, 3817 (2004).
40. A. S. Barnard, S. P. Russo, and I. K. Snook, *Nano Lett.* 3, 1323 (2003).
41. A. S. Barnard, S. P. Russo, and I. K. Snook, *J. Nanosci. Nanotechnol.* 4, 151 (2004).
42. A. S. Barnard, S. P. Russo, and I. K. Snook, *J. Comput. Theor. Nanosci.* 2, 68 (2005).
43. J.-Y. Raty and G. Galli, *Nat. Mater.* 2, 792 (2003).
44. A. S. Barnard, N. A. Marks, S. P. Russo, and I. K. Snook, *MRS Symp. Proc.* 740, 13.4.1 (2003).
45. A. S. Barnard, S. P. Russo, and I. K. Snook, *J. Comput. Theor. Nanosci.* 2, 180 (2005).
46. A. S. Barnard, *Rev. Adv. Mater. Sci.* 6, 94 (2004).
47. A. S. Barnard, S. P. Russo, and I. K. Snook, *J. Chem. Phys.* 118, 10725 (2003).
48. A. S. Barnard, S. P. Russo, and I. K. Snook, *Phil. Mag.* 83, 2311 (2003).
49. D. N. Laikov and Y. A. Ustyniyuk, *Russ. Chem. Bull., Int. Ed.* 54, 820 (2005).
50. A. Lewandowski and A. R. Merchant, 17th National Congress, Australian Institute of Physics, Brisbane, December (2006).
51. J. E. Dahl, S. G. Liu, and R. M. K. Carlson, *Science* 299, 96 (2003).
52. Y. V. Butenko, P. R. Coxon, M. Yeganeh, A. C. Brieva, K. Liddell, V. R. Dhanak, and L. Šiller, *Diam. Rel. Mater.* 17, 962 (2008).
53. A. R. Muniz, T. Singh, E. S. Aydil, and D. Maroudas, *Phys. Rev. B* 80, 144105 (2009).
54. G. Kern and J. Hafner, *Phys. Rev. B* 56, 4203 (1997).
55. P. G. Lurie and J. M. Wilson, *Surf. Sci.* 65, 453 (1977).
56. F. Maier, R. Graupner, M. Hollering, L. Hammer, J. Ristein, and L. Ley, *Surf. Sci.* 443, 177 (1999).
57. B. B. Pate, *Surf. Sci.* 165, 83 (1986).
58. J. Furthmuller, J. Hafner, and G. Kresse, *Phys. Rev. B* 53, 7334 (1996).
59. A. V. Hamza, G. D. Kubiak, and R. H. Stulen, *Surf. Sci.* 237, 35 (1990).
60. T. Evans and J. E. Field (eds.), *The Properties of Diamond*, Academic Press, New York (1979), p. 403.
61. S. Hong and M. Y. Chou, *Phys. Rev. B* 55, 9975 (1997).
62. M. D. Winn, M. Rassinger, and J. Hafner, *Phys. Rev. B* 55, 5364 (1997).
63. S. H. Yang, D. A. Drabold, and J. B. Adams, *Phys. Rev. B* 48, 5261 (1993).
64. C. Su and J.-C. Lin, *Surf. Sci.* 406, 149 (1998).
65. J. Ristein and R. Graupner, *Adv. Solid State Phys.* 36, 77 (1997).
66. K. Bobrov, B. Fiskeer, H. Shechter, M. Folman, and A. Hoffman, *Diam. Rel. Mater.* 6, 736 (1997).
67. K. C. Pandey, *Phys. Rev. B* 25, 4338 (1982).
68. D. R. Alfonso, D. A. Drabold, and S. E. Ulloa, *Phys. Rev. B* 51, 14669 (1995).
69. C. Z. Wang, K. M. Ho, M. D. Shirk, and P. A. Molian, *Phys. Rev. Lett.* 85, 4092 (2000).
70. G. Kern, J. Hafner, and G. Kresse, *Surf. Sci.* 366, 445 (1996).
71. S. Evans, *The Properties of Natural and Synthetic Diamond*, edited by J. E. Field, Academic Press, New York (1992), p. 181.
72. G. D. Kubiak, A. V. Hamza, R. H. Stulen, E. C. Sowa, K. W. Kolasinski, and M. A. Van Hove, *Proceedings of the Second International Conference, New Diamond Science and Technology*, edited by R. Messier, J. T. Glass, J. E. Butler, and R. Roy, Materials Research Society, Pittsburgh, PA (1991), p. 21.
73. T. Schaich, J. Braun, J. P. Toennies, M. Buck, and C. Woll, *Surf. Sci.* 385, L958 (1997).
74. C. Su, K.-J. Song, Y. L. Wang, H.-L. Lu, T. J. Chuang, and J.-C. Lin, *J. Chem. Phys.* 107, 7543 (1997).
75. Y. Mitsuda, T. Yamada, T. J. Chuang, H. Seki, R. P. Chin, J. Y. Huang, and Y. R. Shen, *Surf. Sci.* 257, L633 (1991).
76. H. Seki, T. Yamada, T. J. Chuang, R. P. Chin, J. Y. Huang, and Y. R. Shen, *Diam. Rel. Mater.* 2, 567 (1993).
77. R. P. Chin, J. Y. Huang, Y. R. Shen, T. J. Chuang, and H. Seki, *Phys. Rev. B* 52, 5985 (1995).
78. J. B. Cui, J. Ristein, and L. Ley, *Phys. Rev. B* 59, 5847 (1999).
79. A. V. Hamza, G. D. Kubiak, and R. H. Stulen, *Surf. Sci.* 206, L833 (1988).
80. K. A. Jackson, *Proceedings of the Second International Conference, New Diamond Science and Technology*, edited by R. Messier, J. T. Glass, J. E. Butler, and R. Roy, Materials Research Society, Pittsburgh, PA (1991), p. 51.

81. Car-Parrinello Molecular Dynamics (CPMD) Consortium, <http://www.cpmc.org/>
82. J. P. Perdew, K. Burke, and M. Ernzerhof, *Phys. Rev. Lett.* 77, 3865 (1996).
83. C. Hättig, A. Hellweg, and A. Köhn, *Phys. Chem. Chem. Phys.* 8, 1159 (2006).
84. U. Kaldor, *Phys. Rev. A* 19, 105 (1979).
85. G. Jungnickel, D. Porezag, T. Frauenheim, M. I. Heggie, W. R. L. Lambrecht, B. Segall, and J. C. Angus, *Phys. Status Solidi A* 154, 109 (1996).
86. R. Astala, M. Kaukonen, R. M. Nieminen, G. Jungnickel, and T. Frauenheim, *Phys. Rev. B: Condens. Matter* 63, 81402 (2001).

Received: 30 March 2010. Accepted: 2 May 2010.